# Hydrodynamics of in-canopy flow in synthetically generated coral reefs under oscillatory wave motion

Patil, Akshay; García-Sánchez, Clara

**DOI**
10.1016/j.coastaleng.2025.104840

**Publication date**
2025

**Document Version**
Final published version

**Published in**
Coastal Engineering

Coastal Engineering 202 (2025) 104840

Contents lists available at ScienceDirect

Coastal Engineering

journal homepage: www.elsevier.com/locate/coastaleng

# Hydrodynamics of in-canopy flow in synthetically generated coral reefs under oscillatory wave motion

Akshay Patil *, Clara García-Sánchez

3D Geoinformation Research Group, Faculty of Architecture and Built Environment, Delft University of Technology, Julianalaan 134, Delft, 2628BL, The Netherlands

ARTICLE INFO

*Keywords:*
Canopy turbulence
Direct numerical simulations
Coral reefs
Wave Boundary Layer

ABSTRACT

The interaction of oscillatory wave motion with morphologically complex coral reefs showcases a wide range of consequential hydrodynamic responses within the canopy. While a large body of literature has explored the interaction of morphologically simple coral reefs, the in-canopy flow dynamics in complex coral reefs are poorly understood. This study used a synthetically generated coral reef over flat topography with varying reef height and frontal and planform density to understand the in-canopy turbulence dynamics. Using a turbulence-resolving computational framework, we found that most of the turbulent kinetic energy dissipation is confined to a region below the top of the reef and above the Stokes boundary layer. The results also suggest that most of the vertical Reynolds stress peaks within this region positively contribute to the down-gradient momentum flux during the wave cycle. These findings shed light on the physical relationships between in-canopy flow and morphologically complex coral reefs, thereby motivating a further need to explore the hydrodynamics of such flows using a scale-resolving computational framework.

## 1. Introduction

Coral reefs exhibit a vital symbiotic relationship with the oceanic environment and its diverse aquatic and biological components, a connection that significantly underpins their overall health and vitality (Lowe and Falter, 2015). Despite their critical role in the coastal oceanic system, global coral reef health has declined over the past few decades due to increased ocean acidification and warming (Caldeira and Wickett, 2003), even though some coral species have the potential to genetically adapt to the heat stress (Selmoni et al., 2024). Consequently, there is a growing scientific interest in understanding the life cycle of corals and the hydrodynamic environment they inhabit. The turbulent oceanic environment provides corals with essential nutrients and supports their overall health and ecosystem. Notably, a pioneering study by Munk and Sargent (1948) demonstrated that coral reefs flourish prominently in areas characterised by effective wave energy dissipation, as it enables faster cycling of nutrients required by the corals. Leveraging this observation, Hearn et al. (2001) proposed a physical model for the nutrient-uptake rates in coral reefs, thus connecting the mass-transfer rate between the hydraulic environment and the underlying benthic organism (i.e., corals) through the turbulent kinetic energy (TKE) dissipation rate. These connections between the hydrodynamics and the coral reef systems motivated a wide range of studies aimed at understanding this crucial ecosystem (Reidenbach, 2004; Falter et al., 2005; Reidenbach et al., 2006; Monismith, 2007; Ribes and Atkinson, 2007). Jones et al. (2008) studied the plume dispersion over fringing coral reefs in O'ahu, Hawaii and observed that the lateral turbulent dispersion coefficients were enhanced due to the interaction of waves and coral roughness. To that end, Nunes and Pawlak (2008) studied the roughness characteristics in O'ahu, Hawaii, to illustrate the connection between the wavenumber spectra and the type of roughness. In another pioneering study to characterise the mass transfer rate as a function of wave strength and coral morphology, Reidenbach et al. (2006) showed that the in-canopy flow increased for both unidirectional and oscillatory flow, thus further enhancing the mass transfer.

With a wide range of studies illustrating the connection between the coral roughness, hydrodynamics, and mass transfer within the coral canopy, more recent studies have tried to better quantify the in-canopy flow features as a function of the requisite independent parameters (Suzuki et al., 2019; Jacobsen and McFall, 2022; Ascencio et al., 2022; Rooijen et al., 2022, to list a few). The central thesis in some of these studies has aimed at modelling the effect of in-canopy turbulence as a porous medium, affecting the flow over it by tuning the inertial and frictional drag parameters. Such flows have been extensively studied as emergent vegetation to consider the transport

* Corresponding author.
*E-mail address:* a.l.patil@tudelft.nl (A. Patil).

https://doi.org/10.1016/j.coastaleng.2025.104840
Received 15 May 2025; Received in revised form 3 July 2025; Accepted 22 July 2025
Available online 5 August 2025

of momentum and scalars within and outside the canopy, with some of the most notable studies summarised by Nepf (2011). To enable such a modelling approach, it is important to understand the turbulence dynamics within the canopy better, as illustrated by pioneering works discussing the flow within such systems (Nepf and Vivoni, 2000; Ghisalberti and Nepf, 2002; Monismith, 2007; Pujol et al., 2013).

Drawing inspiration from the above-mentioned studies and the need to understand the turbulence dynamics within the coral canopies, this study aims to understand the effect of varying coral height and flow strength on the flow within the coral canopy. To achieve this, we model the flow over synthetically generated coral reefs on flat topography to demonstrate the utility of the computational framework. The paper first introduces the details of the computational model and simulation parameters, along with the convergence history of the flow statistics. This is followed by a detailed discussion of the phase-averaged flow response and the turbulence dynamics. At the end, a summary of our conclusions is presented, and future work directions are briefly discussed.

## 2. Methodology

### 2.1. Governing equations and discretisation

Assuming small wave-steepness, the flow over the coral(s) can be modelled similarly to that of a sinusoidal pressure gradient driving the flow in shallow waters over benthic boundaries (Nielsen, 1992; Ozdemir et al., 2014; Ghodke and Apte, 2016). The governing equations are thus given by

$$\partial_t u_i + \partial_j \left(u_j u_i\right) = -\frac{1}{\rho_0}\partial_i p + \nu \partial_j \partial_j u_i + U_b \omega \cos(\omega t)\delta_{i1} + \mathcal{F}_{\mathrm{IBM}}, \tag{1}$$

subjected to the incompressible continuity equation given by

$$\partial_i u_i = 0, \tag{2}$$

where $\partial_t \equiv \frac{\partial}{\partial t}$ is the time derivative, $t$ is time, $\partial_i \equiv \frac{\partial}{\partial x_i}$ is the partial derivative in space, $x_i$ represents the coordinate axis where $i = 1, 2, 3$ correspond to the streamwise, spanwise, and vertical directions, respectively, $u_i$ is the velocity vector, $\rho_0$ is the density of the fluid, $p$ is the pressure, $\nu$ is the kinematic viscosity, $U_b$ is the maximum wave orbital velocity, $\omega \equiv 2\pi/T_w$ is the wave frequency where $T_w$ is the wave period, $\delta_{ij}$ is the Kronecker delta, and $\mathcal{F}_{\mathrm{IBM}}$ is the immersed boundary force. This paper uses the summation convention for tensor notation such that any two repeating indices are summed over. Using the non-dimensional velocity scale as $u_{i_*} \equiv u_i/U_b$, length scale as $x_{i_*} \equiv x_i/k_s$ where $k_s$ is the representative maximum height of the coral(s), time scale as $t_* \equiv t\omega$, and pressure scaling as $p_* \equiv p/(\rho_0 U_b^2)$ gives the non-dimensional momentum equations (excluding the immersed boundary force)

$$\partial_{t_*} u_{i_*} + \frac{U_b}{\omega k_s}\partial_{j_*}(u_{j_*}u_{i_*}) = -\frac{U_b}{\omega k_s}\partial_{i_*} p_* + \frac{\nu}{k_s^2 \omega}\partial_{j_*}\partial_{j_*}u_{i_*} + \cos(t_*)\delta_{i1}. \tag{3}$$

Defining $A = U_b/\omega$ as the wave particle semi-excursion length (Nielsen, 1992, equation 1.1.2), Eq. (3) can be written as

$$\partial_{t_*} u_{i_*} + \frac{A}{k_s}\partial_{j_*}(u_{j_*}u_{i_*}) = -\frac{A}{k_s}\partial_{i_*} p_* + \left(\frac{\nu}{k_s U_b}\right)\left(\frac{A}{k_s}\right)\partial_{j_*}\partial_{j_*}u_{i_*} + \cos(t_*)\delta_{i1},$$

which can be alternatively written after defining the roughness Reynolds number ($Re_k^b \equiv (U_b k_s)/\nu$) and the relative-roughness ($\Gamma \equiv A/k_s$), which is the inverse of the Keulegan–Carpenter number (Nielsen, 1992) as

$$\partial_{t_*} u_{i_*} + \Gamma \partial_{j_*}(u_{j_*}u_{i_*}) = \Gamma\left(-\partial_{i_*} p_* + \frac{1}{Re_k^b}\partial_{j_*}\partial_{j_*}u_{i_*}\right) + \cos(t_*)\delta_{i1}. \tag{4}$$

Eq. (4) suggests that flow dynamics in the leading order are affected by $\Gamma$ and $Re_k^b$ for this problem setup. Consequently, in this study, we focus on understanding how changing the relative roughness and the roughness-Reynolds number affect the flow parameters in a wave boundary layer flow over a synthetically generated collection of corals on flat topography. It is clear from this form of the equation that the temporal acceleration balances the oscillatory pressure gradient, while the advection of momentum balances the pressure and diffusion of the momentum, scaled by the relative roughness and the Reynolds number, in the region far away from the wall. While the in-canopy flow response does not necessarily exhibit identical balance as the region far away from the wall, it acts to set the bottom boundary condition for the outer flow (Jiménez, 2004; Monti et al., 2020). The emphasis on the dissipation rate is primarily motivated by the limitations in measuring higher-order moments of the velocity vector in experimental and/or in-situ measurements; however, decent estimates for the dissipation rate can be made, assuming isotropy within the inertial range (Reidenbach et al., 2006), thus providing a link between the nutrient transport and the hydrodynamics as discussed in Hearn et al. (2001).

The momentum and continuity equations are discretised over a staggered grid using a second-order accurate finite differences in space. At the same time, the time integration is done using the fractional-step algorithm and a Runge–Kutta method that is third-order accurate in time (Orlandi, 2000; Moin and Verzicco, 2016). To introduce the roughness elements (i.e., corals), a volume-penalisation immersed boundary method (*VIBM*) as introduced by Scotti (2006) is used such that Eq. (4) has an additional body force $\mathcal{F}_{IBM}$ on the right-hand side. Using the signed distance field (SDF), the flow is forced to satisfy the no-slip and no-penetration conditions at the interface of the geometry (SDF equals 0). With the aid of the SDF, close to the solid-fluid interface, the volume fraction is not set to binary values of 0 or 1 and instead smeared across three grid cells continuously, such that the velocity steadily approaches the boundary. This results in less severe dispersive numerical errors at the cost of local non-enforcement of the no-normal flow through the solid interface. This is, however, an acceptable compromise given the simplicity of the immersed boundary method and has been validated extensively to demonstrate its validity for high-Reynolds number flows (Scotti, 2006; Yuan and Piomelli, 2015). The advection term is discretised explicitly, while the viscous term is discretised implicitly in the vertical direction to eliminate the strict time-step limitation. The pressure Poisson equation is solved efficiently using a Fast Poisson solver since the streamwise and spanwise directions are homogeneous (McKenney et al., 1995). All the simulations were carried out on the Snellius supercomputer on the Genoa partition, containing 96 computing cores on a single node. For cases c1, c2, c5, and c6, 8 computing cores were used; for the rest, two nodes with 192 computing cores were used.

To understand the flow response subjected to various synthetic coral collection configurations, we ran six simulations as detailed in Table 1. For all cases, the computational domain is $15k_s \times 15k_s$ in the streamwise and spanwise directions, respectively, and is discretised using 512 grid points. In the vertical direction, the grid is uniformly distributed over the coral height $k_s$ using $N_k$ number of cells, while above $k_s$ the grid is stretched using a hyperbolic tangent stretching function. Fig. 1(a) presents the same data on a phase plot with the $x$-axis marking the wave Reynolds number (i.e., the strength of the wave) and the $y$-axis marking the relative roughness ($\Gamma$). In this formulation, $\omega$ and $U_b$ appear both on the x- and the $y$-axis of the parameter space as shown in Fig. 1. As a result, to obtain a consistent non-dimensional timescale (i.e., $\omega$ to shear velocity and viscosity-based time scale), we vary the maximum wave orbital velocity ($U_b$) and the maximum roughness height ($k_s$) to change the non-dimensional parameters. One could alternatively vary the viscosity to change the wave Reynolds number; however, since the wave boundary layer thickness also varies with the changes in viscosity, in this case, this option was discarded to have a consistent formulation of the parameters. Ultimately, this results in different roughness-Reynolds numbers ($Re_k^b$) for identical wave-Reynolds numbers ($Re_w$) between cases c1, c2, c3, c4, and cases c5, c6, respectively. As seen in Table 1, the choice of such a parameter space leads to varying submergence ratios defined as the ratio of

**Table 1**
Simulations carried out in this paper. For reference, case c4 is similar to a wave height of 0.13 m with a water depth of 5 m and a wave period of 15 s using the linear wave theory.

| Case name | $Re_w \equiv \frac{U_b^2}{\omega\nu}$ | $Re_k^b \equiv \frac{U_b k_s}{\nu}$ | $\Gamma \equiv \frac{A}{k_s}$ | $U_b$ [m/s] | $T_w$ [s] | $k_s$ [m] | $N_{x_3}$ | $N_k$ |
|---|---|---|---|---|---|---|---|---|
| c1 | 351 | 351 | 1 | 0.021000 | 5 | 0.0167 | 128 | 40 |
| c2 | 351 | 351 | 1 | 0.012125 | 15 | 0.0289 | 128 | 50 |
| c3 | 3990 | 3990 | 1 | 0.070809 | 5 | 0.0564 | 256 | 120 |
| c4 | 3990 | 3990 | 1 | 0.040882 | 15 | 0.0976 | 256 | 150 |
| c5 | 351 | 702 | 0.5 | 0.021000 | 5 | 0.0334 | 128 | 60 |
| c6 | 351 | 702 | 0.5 | 0.012125 | 15 | 0.0579 | 128 | 60 |

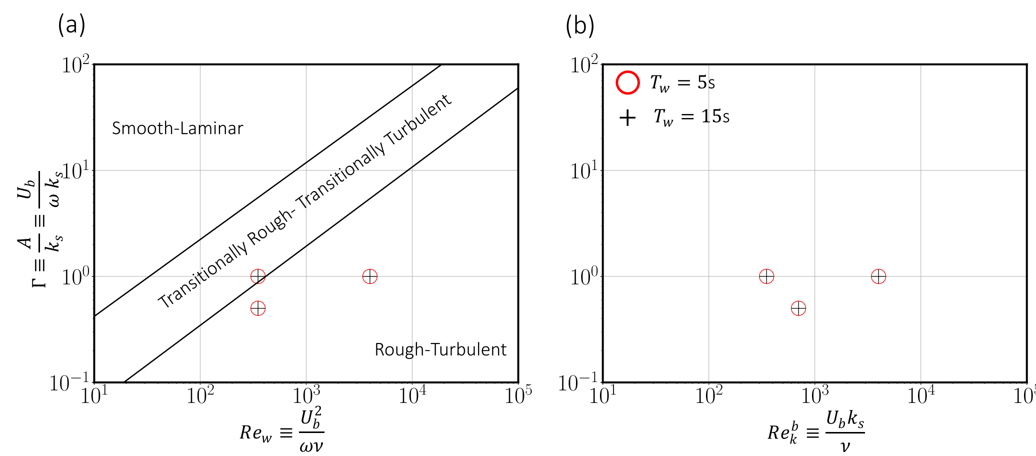


**Fig. 1.** (a) Simulations carried out in this paper with the wave Reynolds number on the $x$-axis and the relative roughness on the $y$-axis. The black solid lines mark the hydraulic and flow classification regimes as discussed in Lacy and MacVean (2016). (b) The same data as panel (a) with the roughness Reynolds number on the $x$-axis. Empty circles mark the cases with a wave period of $T_w = 5$ s (i.e., cases c1, c3, and c5), while the plus symbols mark the cases with a wave period of $T_w = 15$ s (i.e., cases c2, c4, and c6).

the coral roughness to the height of the water column ($k_s/H$), in this case, the height of the water column corresponds to the height of the computational domain. As a result, the $x_3$ coordinate of the computational domain is varied such that the top boundary condition does not severely affect the in-canopy flow.

The choice of flow conditions is largely constrained by the grid resolution needed to accurately represent the requisite flow features. Additionally, resolving coral reef roughness requires a uniform grid throughout the vertical extent, making conventional grid stretching unsuitable for this configuration. While previous studies have focused on flow dynamics with relatively small roughness-to-channel height ratios (Ghodke and Apte, 2016, 2018; Dunbar et al., 2023), this setup is not feasible in this work due to the relatively large coral roughness height. As a result, achieving realistic wave Reynolds numbers is not possible, and the maximum considered in this study is a modest $Re_w = 3990$. Additionally, since the coral reef is synthetically generated, the potential range of values for $A/k_s$ cannot be matched identically as observed in situ/experimental conditions. The goal is not to replicate field conditions exactly but to examine a simplified case that clarifies how coral reef heterogeneity influences flow dynamics.

### 2.2. Coral bed generation

The coral bed is generated using a randomly (uniform distribution) sampled collection of three coral geometries, namely *Acropora cervicornis*, *Acropora secale*, and *Goniastrea favulus*. The 3D scans for the corals were obtained from the Smithsonian coral scan repository (https://3d.si.edu/corals) that provides manifold geometries requiring minimal to no geometry repair through the watertight 3D stereolithography (stl) file format. The coral geometries are then randomly sampled, translated, and rotated within the defined computational limits to generate a contiguous coral stl. The translation, rotation, and coral index choices are uniformly sampled from the prescribed spatial, rotational, and coral index limits, respectively. While the individual coral geometries are watertight, the collection of corals generated using the sampling approach is not collectively watertight, as it is ambiguous to define watertightness for non-manifold geometries. Thus, the collection of corals is wrapped using the wrapwrap (https://github.com/ipadjen/wrapwrap) application built on the alpha-wrap algorithm developed by Alliez et al. (2023). Choosing the input values for the relative alpha ($\alpha = 1500.0$) and relative offset ($\beta = 2000.0$), wrapwrap generates a single watertight coral geometry and reduces the total file size, making the SDF computation less memory intensive. The watertight geometry ensures a non-degenerate SDF using the stl2sdf generator, which uses a local sampling method to generate the SDF. Detailed scaling results for stl2sdf are discussed in Appendix B. Fig. 2 illustrates the typical stochastically generated corals used for four of the six cases in this paper. Using the geometry translation, the maximum height of the corals can be exactly set as detailed in Table 1. This computational workflow allows the generation of stochastic coral reefs over flat terrains with specified extents and maximum height. The code has been since updated to handle non-flat topography using Perlin noise (Perlin, 1985); however, in this paper, we will only discuss corals over flat terrains.

Fig. 3a shows the vertical profile of the planform solid fraction ($\phi_c^p$); for all cases, $\phi_c^p$ peaks close to 0.3. Here, the planform solid fraction is defined as the ratio of the area occupied by the coral to the total available planform area at a given distance above the wall. Fig. 3b shows the streamwise profile of the frontal solid fraction ($\phi_c^f$), where, for different cases, the peak value varies from 0.1 to 0.3. In addition to the coordinate-dependent area fractions, the frontal and planform projected areas of the solid fraction (corals in this case) are important indicators. Thus, Table 2 presents a detailed summary of the frontal and planform projected areas for the various cases. It is clear from Table 2 that despite the control over the height and layout, there is a large variation in the frontal area occupied by the corals, where it ranges from about 0.2850 (minimum) to 0.6235 (maximum). As a result, despite the tight control over the coral height, changes in all the requisite parameters of interest that affect the flow dynamics cannot be directly controlled when designing a parametric sweep.

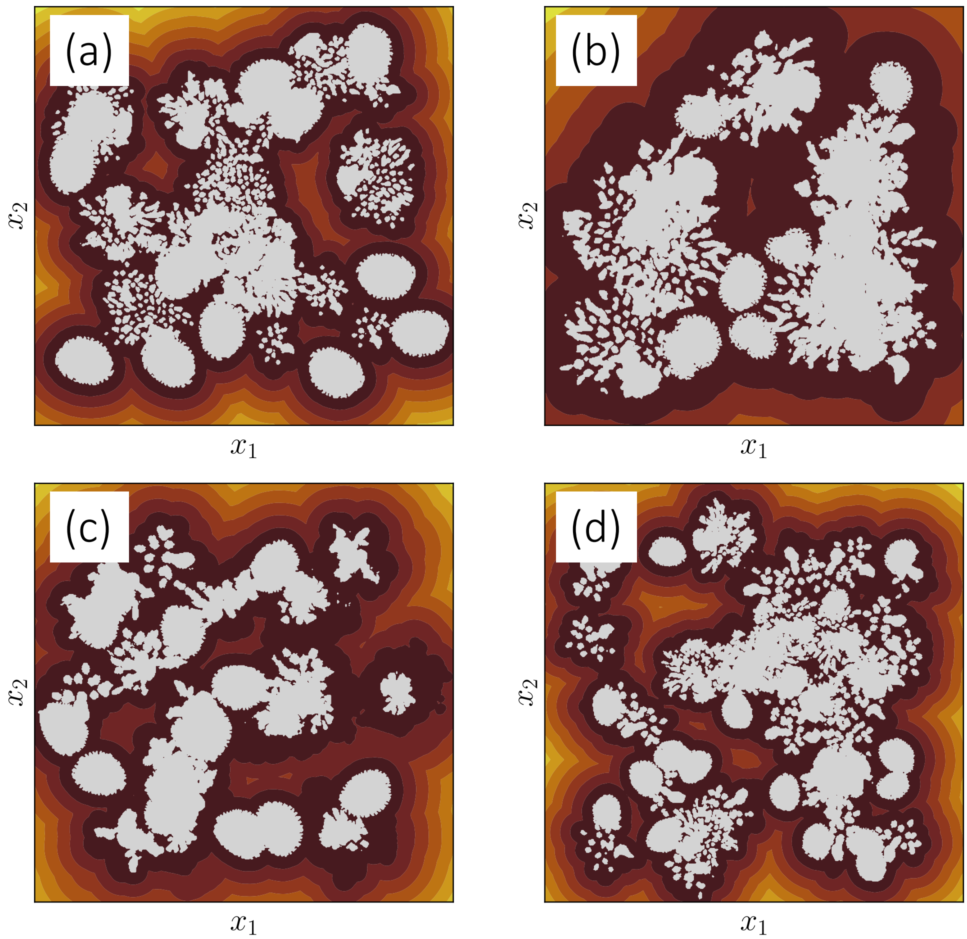


**Fig. 2.** Top view of the stochastically generated corals sliced at $k_s/2$ for four of the six cases discussed in this work. The light grey colour marks the corals, while the shading marks the positive SDF.

**Table 2**
Non-dimensional planform and the frontal area occupied by the corals for the cases simulated in this paper. The last column also details the non-dimensional vertical extend of the computational domain ($L_z$).

| Case name | $\frac{A_c^p}{A^p}$ | $\frac{A_c^f}{A^f}$ | $\frac{A_c^p}{A_c^f}$ | $\frac{L_z}{\sqrt{2\nu/\omega}}$ |
|---|---|---|---|---|
| c1 | 0.4456 | 0.2850 | 3.658 | 80 |
| c2 | 0.5250 | 0.4273 | 2.875 | 45 |
| c3 | 0.4638 | 0.6100 | 4.285 | 118 |
| c4 | 0.4655 | 0.5764 | 3.412 | 90 |
| c5 | 0.5250 | 0.4303 | 2.855 | 80 |
| c6 | 0.4207 | 0.6235 | 4.072 | 65 |

### 2.3. Convergence of turbulence statistics and additional parameters

All the cases are run for a total of 60 wave periods, with the results being stored at every $\frac{T_w}{20}$ s to capture the turbulence statistics over the entire wave period sufficiently. To understand the convergence of turbulent statistics, we use the volume-averaged estimates of the various flow quantities of interest. For a given flow quantity of interest $f_i$, the planform-average is defined as

$$\langle f_i \rangle(x_3, t) = \frac{1}{A_f(x_3)} \int_{A_f(x_3)} f_i(x_1, x_2, x_3, t) dA, \tag{5}$$

where $A_f$ is the planform area occupied by the fluid (i.e., the area occupied by the non-light grey region in Fig. 2) and the volume-average is the vertical-integral of the planform-averaged quantity given by

$$\langle f_i \rangle_v(t) = \frac{1}{H} \int_0^H \langle f_i \rangle(x_3', t) dx_3', \tag{6}$$

where $H$ is the height over which the vertical integration is carried out. Additionally, the flow quantity $f_i$ can be decomposed as

$$f_i(x_1, x_2, x_3, t) = \tilde{f}_i(x_1, x_2, x_3, \omega t) + f_i'(x_1, x_2, x_3, t), \tag{7}$$

where the first term on the right-hand side is the phase-averaged component of $f_i$, while the second term on the right-hand side is the turbulent component of $f_i$, and the phase average is given by

$$\tilde{f}_i(x_1, x_2, x_3, \omega t) = \frac{1}{N_w} \sum_{j=1}^{N_w} f_i(x_1, x_2, x_3, t + jT_w) \tag{8}$$

The phase-averaging component in Eq. (7) can be further decomposed using the planform-averaging operator. Thus, Eq. (7) can be written as

$$f_i(x_1, x_2, x_3, t) = \langle \tilde{f}_i \rangle(x_3, \omega t) + \hat{f}_i(x_1, x_2, x_3, \omega t) + f_i'(x_1, x_2, x_3, t), \tag{9}$$

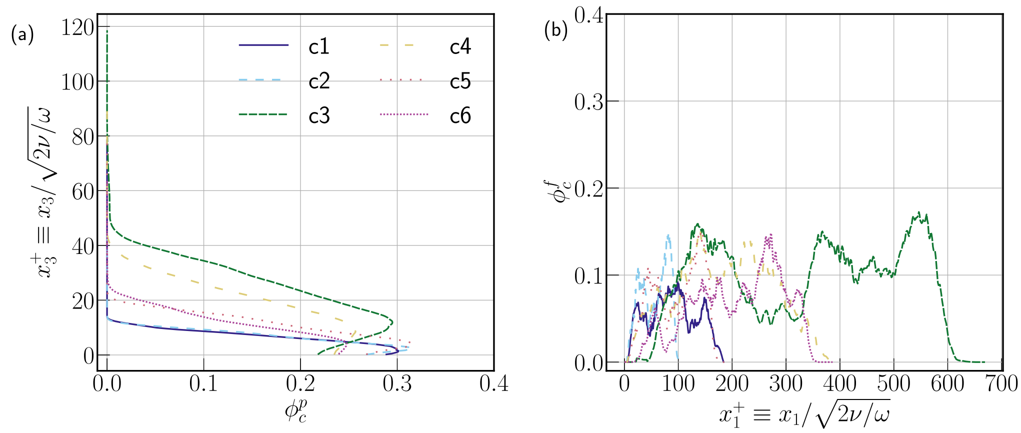


**Fig. 3.** (a) Planform area fraction occupied by the coral (solid) as a function of the vertical coordinate. The two columns in the legend correspond to the varied relative roughness parameter ($\Gamma$), where the first column has $\Gamma = 1.0$ and the second column has $\Gamma = 0.5$ for an identical wave Reynolds number. (b) Frontal area fraction occupied by the coral (solid) as a function of the streamwise coordinate. Colour scheme for the lines is the same as panel (a).

where the second term on the right-hand side of Eq. (9) is the dispersive velocity component defined as

$$\hat{f}_i(x_1, x_2, x_3, \omega t) = \widetilde{f}_i(x_1, x_2, x_3, \omega t) - \langle \widetilde{f}_i \rangle(x_3, \omega t). \tag{10}$$

In this paper, the triple velocity decomposition as defined in Eq. (9) will be used to understand the phase variability and compute the turbulence statistics. Specifically, the sum of the dispersive and turbulent components will be used to estimate the convergence of the turbulence statistics. This is done in order to understand how the relevant scale of the flow converges as a function of the number of samples (i.e., the number of waves), as the mean flow converges relatively quickly when compared to the fluctuating and dispersive components. Additionally, the phase- and planform-averaged velocity components can be computed once the three-dimensional velocity and pressure fields are obtained. Using the velocity decomposition proposed in Eq. (9), the sum of the turbulent and the dispersive components can be readily computed as a function of time.

The time evolution of the various flow quantities of interest for case c2 can be seen in Fig. 4 where the + marker denotes non-dimensionalisation using the maximum friction (i.e., or shear) velocity ($u_\tau$), the kinematic viscosity ($\nu$), and the von Kármán constant ($\kappa$) taken to be 0.41 where appropriate. The friction velocity for all the cases is defined as

$$u_\tau = \sqrt{\max\left[-\langle u_1' u_3' \rangle_v(t)\right]}. \tag{11}$$

The choice for this definition is primarily motivated by the limitations of the computational methodology used in this study. Specifically, since a volume penalising IBM is used, the volumetric forcing applied in the solid region is not stored at every time step to calculate the total force exerted, which limits the ability to obtain the shear stress at the wall. While methods do exist to obtain this force as detailed in Yuan and Piomelli (2015), the computational method did not have these capabilities implemented to extract meaningful force values on the coral canopy. As a result, the friction velocity definition is based on the vertically integrated value considered in this work. Based on the temporal evolution of the mean flow and the turbulence statistics as shown in Fig. 4, case c2 converges after 30 wave periods for both the mean flow and the turbulence statistics. The TKE and the TKE dissipation rate converge relatively quickly by around 15 wave periods; however, the correlations between the streamwise and vertical velocity components take relatively longer to converge, as seen in Fig. 4, in addition to exhibiting some variations over time. As a result, when presenting the phase averages, the first 30 wave periods for all the turbulence statistics are discarded, and the phase averages are computed for the last 30 wave periods. Similar trends were observed for all the other cases detailed in Table 1, as case c2; hence, for the sake of brevity, the convergence history for all the other cases will not be discussed. As detailed in Appendix A, the TKE dissipation rate scales with a pre-factor $\Gamma/Re_k^b$; as a result, it is expected that for identical values of $\Gamma$, the TKE dissipation rate contribution decreases with increasing $Re_k^b$. It is important to note that this behaviour is dependent on how the parameters are non-dimensionalised, while the dimensional values for TKE and the TKE dissipation rate typically increase with increasing values of $Re_k^b$. However, as discussed in Pomeroy et al. (2023), the area fraction of the corals also plays an important role in flow response above and within the canopy. As a result, the solid fraction, projected frontal, and planform areas are computed for each of the simulation cases carried out in this paper as shown in Fig. 3 and detailed in Table 2. Here, $A_c^p$ is the planform area occupied by the corals, $A^p$ is the total available planform area, $A_c^f$ is the frontal area occupied by the corals, and $A^f$ is the total frontal area available.

## 3. Results and discussions

### 3.1. Phase averaged velocity

For a far-field velocity given by $u(\infty, t) = U_b \sin(\omega t)$ and no-slip at the wall $u(0, t) = 0$ over a flat wall without any roughness (also famously known as a variation of the Stokes' second problem); the phase-averaged velocity is given by Stokes (1851)

$$\widetilde{u}(z, t) = U_b \sin(\omega t) + U_b \exp(-Kz) \sin(Kz - \omega t), \tag{12}$$

where $K \equiv \sqrt{\omega/(2\nu)}$ and $\widetilde{u}(z, t)$ is the phase- and planform-averaged velocity. It is important to note that the far-field velocity follows a $\sin(\omega t)$ as the driving oscillatory pressure gradient follows a $\cos(\omega t)$ as per Eq. (3). To understand the effect of the coral roughness, the velocity deficit $\widetilde{u}_d(z, t)$ can be defined by

$$\widetilde{u}_d(z, t) = \widetilde{u}(z, t) - \langle \widetilde{U}_1 \rangle(z, t), \tag{13}$$

where the first term on the right-hand side of Eq. (13) is the Stokes' solution for a flat wall using Eq. (12) and the second term on the right-hand side is the phase- and planform-averaged velocity for a flat wall with corals obtained using the numerical method. Fig. 5 shows the numerically obtained velocity profiles for the cases detailed in Table 1 using the solid black lines, while Fig. 6 shows the deficit velocity marked in solid green lines. As defined in Eq. (13), larger deficit components suggest smaller in-canopy flow velocities when the corals are present over the flat wall. Since the planform area for all the cases is similar, most of the differences observed in Fig. 5 can be understood through the varying frontal area detailed in Table 2. Specifically, case c2 has a relatively large frontal area ratio, leading to a smaller in-canopy velocity magnitude compared to the rest of the cases presented

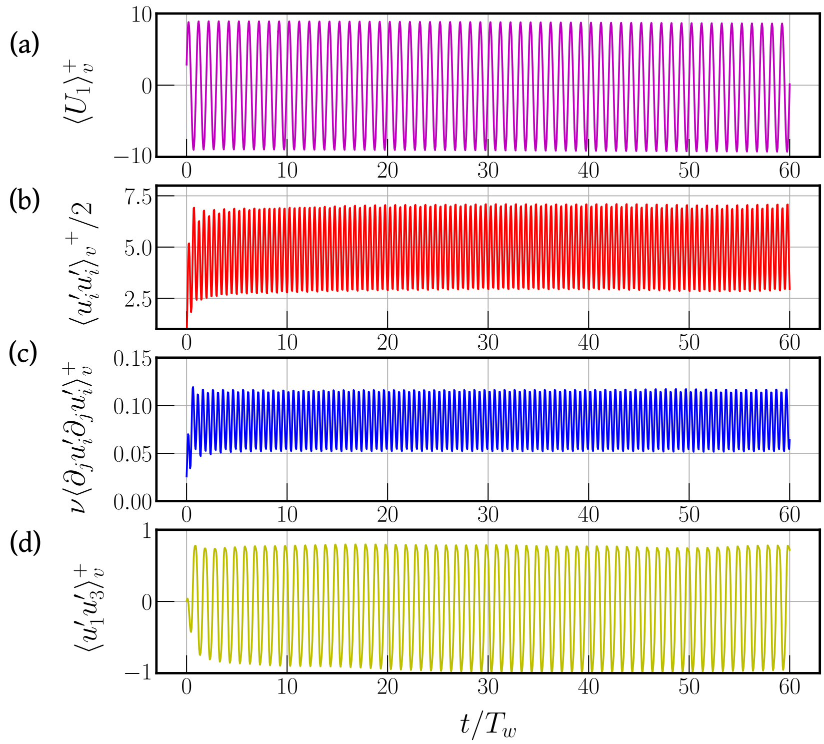


**Fig. 4.** Time evolution of the volume-averaged flow statistics for case c2. All panels are volume-averaged quantities: (a) wave velocity, (b) turbulent kinetic energy (TKE), (c) TKE dissipation rate, and (d) Reynolds stress. The $X$-axis for all the panels corresponds to the non-dimensional time normalised using the wave period (i.e., the $x$-axis corresponds to the number of wave periods). Panel (a) is normalised using $u_\tau$, panels (b) and (d) are normalised using $u_\tau^2$, and panel (c) is normalised using $u_\tau^4/(\kappa\nu)$. For case c2, the friction velocity is $u_\tau = 0.0024$ m/s using Eq. (11).

in Fig. 5. While the differences between the in-canopy velocities are small for the other cases, a weak dependence on the morphological parameters can be observed in the wave velocity. Although not shown here, the numerical and analytical solutions detailed in Eq. (12) are in agreement away from the coral roughness as indicated by the vertical dotted blue lines at $U_b = \pm 1.0$. A substantial amount of the velocity profile is observed to be affected by the presence of the coral roughness below the coral canopy, as detailed by the relatively larger deficit velocity components for each of the cases.

To further illustrate the effect of corals on the phase-averaged velocity, the velocity profiles ($\langle \widetilde{U}_1 \rangle$) are vertically integrated over the height of the corals (i.e., horizontal dashed-red line in Fig. 5) and normalised with the vertically integrated Stokes' solution and maximum wave orbital velocity in Fig. 7. Case c6 seems to be the least affected by the presence of corals, where the velocity is observed to be consistently higher than that of the other cases. Cases c1, c4, and c5 are observed to undergo similar attenuation of the velocity magnitude during the acceleration and deceleration part of the wave phases, while cases c2 and c3 are affected the most by the presence of corals. The velocity magnitude is substantially attenuated at the peak values, with case c2 showing a reduction of over 40% while case c6 experiences an attenuation of about 10%–15% when compared to the free-stream wave orbital velocity.

While the phase-averaged velocity shows a significant dependence on the coral geometry and the wave Reynolds number, the time-averaged Reynolds stress components as seen in Fig. 8 show a relatively consistent trend across the six cases considered in this study. There is a clear dependence on the intensity of the rms velocity profiles on the wave Reynolds number, such that cases c1, c2, c5, and c6 exhibit relatively larger rms velocity magnitudes when compared to cases c3 and c4. This difference is found to be relatively consistent within the canopy layer defined as the region between the two horizontal lines in Fig. 8 given by

$$\mathcal{L}_c = \beta_s \frac{k_s}{H} \gtrapprox x_3 < \frac{k_s}{H}, \tag{14}$$

where $\mathcal{L}_c$ is defined as the canopy layer and the fraction $\beta_s = 0.35$ marks the approximate location where the spanwise and vertical rms velocity components are approximately equal in magnitude. Specifically, the spanwise and vertical rms velocity components are observed to be approximately equal to $u_\tau$. Despite the difference in the roughness-Reynolds number between cases c1, c2 and c5, c6, no discernible trend was observed for the rms velocity components. Cases c3 and c4 consistently show lower streamwise rms velocity profiles within the canopy region, illustrating the influence of the wave Reynolds number on the flow above the coral roughness compared to the other cases. The spanwise and vertical rms velocity components are 1.0–1.2 times $u_\tau$ while below the canopy layer, the vertical rms velocity components develop relatively slowly compared to the spanwise rms velocity component, similar to the trend observed in sheared flows (Pope, 2000). For all the cases discussed in this study, there is a consistent peak for the streamwise rms velocity component just above $\delta_s$, beyond which the streamwise rms velocity decreases, with most of the peak value showcased inside the canopy region. It must be noted that during the wave phase reversal, the velocities go through zero; consequently, both the numerator and denominator plotted on the $y$-axis of Fig. 7(a) become singular. This also explains why the differences start to become large, mainly because of the way the data is presented. Fig. 7(b) demonstrates a more discernible trend for the data. These observations are not universal since the synthetic coral geometry is generated using individual corals that stay the same across the cases discussed in Table 1.

Consequently, generalisations should be cautiously made given the relatively small sample size for the coral geometries and low wave Reynolds number used in this study. Despite these limitations, the trend in the rms velocity profiles and bulk velocity profiles observed seems to suggest that the heterogeneous composition of the synthetic coral geometries leads to a consistent flow response despite relatively large variations in the morphological characteristics when the appropriate scaling parameters are used. This hypothesis will be tested against other

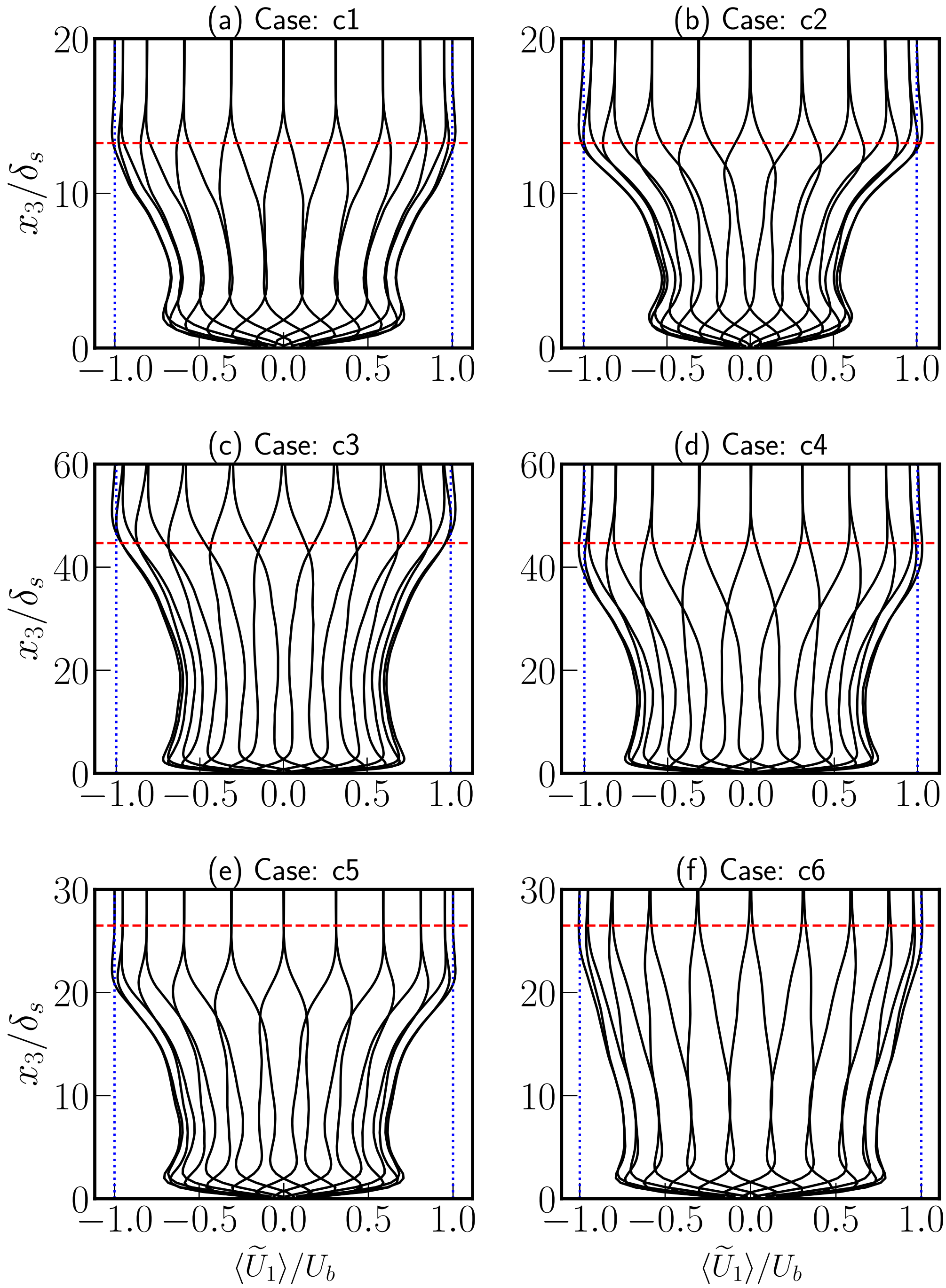


**Fig. 5.** Phase- and planform-averaged velocity profiles for all cases marked using solid-black lines. Vertical blue lines mark the maximum wave orbital velocity for each of the cases, while the horizontal dashed line marks the maximum height of the coral (i.e., $k_s/\delta_s$). Please note the difference in the $y$-axis extents across the various sub-plots presented in this figure.

turbulence parameters in the following sections to better understand the similarities and differences observed across the cases presented in Table 1.

The inner-scaled forcing frequency is given by $\omega^+ \equiv \omega\nu/u_\tau^2$, and Table 3 lists the forcing frequency for all the cases. As detailed by Jelly et al. (2020), for a wave forcing frequency that satisfies the condition $\omega^+ > 0.04$, the turbulence in the flow can be assumed to be in a state of 'frozen' turbulence. Except for cases c3 and c4, all the cases follow the 'frozen' turbulence condition, which suggests that during the wave's peak turbulence generation phase, any generated turbulence will be advected by the flow (Taylor, 1938). In this context, peak turbulence generation refers to the production of turbulent kinetic energy through the energy extraction from the mean strain rate via the Reynolds stress terms, which are then transported by various mechanisms (Pope, 2000). In the case of periodic forcing over rough walls, turbulence production can occur via two primary mechanisms, namely the mean strain supplying TKE through a classical down-gradient cascade and the wake production by the coral roughness that generates turbulence

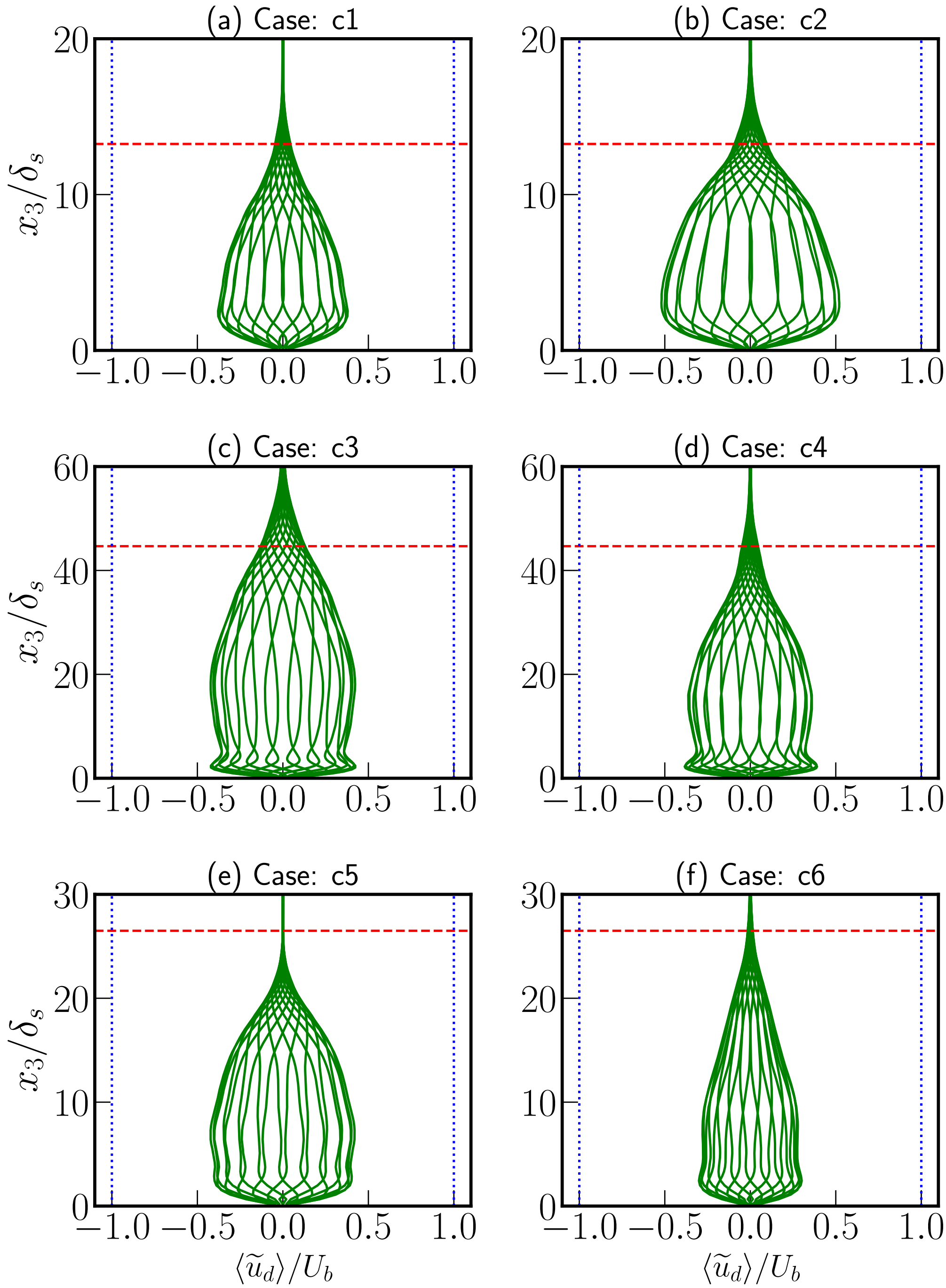


**Fig. 6.** Phase- and planform-averaged deficit velocity profiles for all cases marked using solid-green lines. Vertical blue lines mark the maximum wave orbital velocity for each of the cases, while the horizontal dashed line marks the maximum height of the coral (i.e., $k_s/\delta_s$). Please note the difference in the $y$-axis extents across the various sub-plots presented in this figure.

at the roughness scale as detailed in Ghodke and Apte (2016, 2018). This suggests that the viscous time scale and the wave time scale are equally important and that the viscous processes occur over the same time scale as the wave period. Thus, during the wave cycle, any generated turbulence is expected to be advected within the system and dissipated subsequently (Lacy and MacVean, 2016). Despite the large variation in the wave period for these two cases, the inner-scaled forcing frequencies are similar, and thus, the rms velocity profiles are identical. Specifically, for case c3, close to the wall, there is a small peak at the height of the Stokes boundary layer and within the canopy region. As for case c4, a similar peak at the Stokes' boundary layer height is observed with a secondary peak within the canopy layer. Consequently, in the following subsection, we will discuss in detail the dynamics of in-canopy turbulence.

### 3.2. Secondary flow structures

Phase- and planform-averaged profile provides a useful means to understand the overall state of the boundary layer in the presence of corals; however, at a given wave phase, there can be small secondary flow structures that can impact the overall dynamics. Fig. 9 compares the flow for case c5, comprising the streamwise and the spanwise velocity components, to illustrate the complex flow features observed within the coral canopy. It is important to specify that there

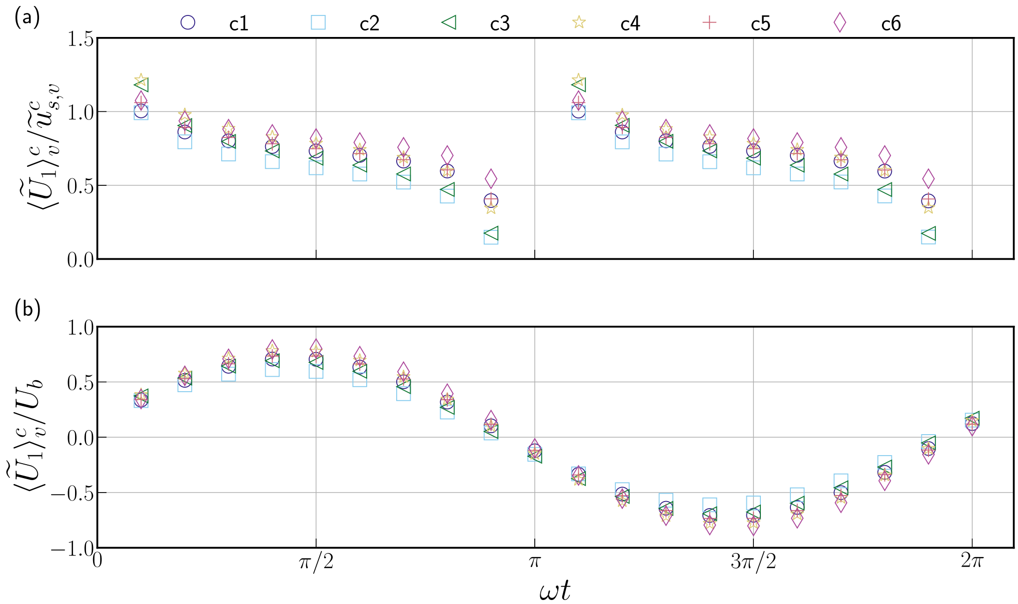


**Fig. 7.** Vertically-integrated, phase- and planform-averaged velocity variations as a function of the wave-phase. Panel a is non-dimensionalised using the Stokes' solution vertically integrated over the coral canopy ($\widetilde{u}_{s,v}^c$), while panel b is non-dimensionalised using the maximum wave orbital velocity.

**Table 3**
Inner-scaled wave frequency for the cases simulated in this study.

| Case name | $\omega^+ \equiv \frac{\omega\nu}{u_\tau^2}$ |
|---|---|
| c1 | 0.435 |
| c2 | 0.292 |
| c3 | 0.011 < 0.04 |
| c4 | 0.014 < 0.04 |
| c5 | 0.398 |
| c6 | 0.430 |

is nothing particularly special about case c5, and it is considered here to illustrate the complex flow features observed in the phase-averaged sense. Similar observations were made for other cases; however, they have not been presented here for brevity. As illustrated in Fig. 9(a)–(j), during the acceleration phase of the wave cycle (see data markers for wave phase locations on the bottom panel of Fig. 14), large in-canopy velocities can be observed as shown in the dark red streamlines that converge between the coral roughness features. Additionally, during the acceleration phase of the wave cycle, a stronger wake region is also seen in panels (c) and (d) behind the coral roughness marked by the dark green streamlines. A relatively strong asymmetry is observed in the phase-averaged behaviour during the acceleration and the deceleration part of the wave cycle, regarding the maximum observed velocities for this particular case. Comparing Fig. 9(c) and (h), which are diametrically opposite in the wave cycle (panel (c) acceleration, panel (h) deceleration), it is observed that a relatively strong flow acceleration marked by the converging red streamlines between the coral canopy results. However, Fig. 9(c) exhibits a relatively stronger acceleration and stronger wake when compared to Fig. 9(h). This can be primarily attributed to the fact that the coral reef itself exhibits a streamwise asymmetry, where the flow during the acceleration cycle (first half of the wave cycle) freely accelerates in the positive streamwise direction (on the right side of Fig. 9(c)), however, is impeded by the series of coral roughness elements during the deacceleration cycle (second half of the wave cycle) thus resulting in a marked difference between the wave cycle. Similar observations can be made when comparing the complex flow features observed during wave phase location $\omega t = 9\pi/10$ (panel e) and $\omega t = 19\pi/10$ (panel j), which show the boundary layer response marked by slow velocities and largely diverging streamlines in the wake regions as the flow velocity is small ($U_b \sim 0$).

Contextualising the flow slightly away from the wall for the same case as shown in Fig. 9(k)–(t), similar observations can be made as discussed above. As the effective canopy density changes with increasing distance away from the wall ($x_3/\delta_s \sim 12.0$), the wall and canopy effects seem to be relatively small and the flow is observed to follow the free stream velocity ($U_b(t)$) as seen in Fig. 9(k), (l), (m), (p), (q), and (r), respectively. In the deceleration part of the wave cycle, as shown in Fig. 9(n), (o), (s), and (t), respectively, the presence of the coral canopy is observed to have a substantial effect in the central part of the canopy marked by strong flow separation. Overall, the in-canopy features illustrate the complexity of the phase-averaged velocity, which is largely impacted by the presence of the coral features, resulting in spatial heterogeneity for modest wave Reynolds numbers as discussed in this work.

Fig. 10 compares the phase-averaged streamlines comprising the spanwise and the vertical velocity components at two distinct locations $x_1/\delta_s = 24.0$ and $x_1/\delta_s = 145.0$ in the flow domain for case c5. These two locations depict relatively different frontal areas in the vertical planes as shown in Fig. 10(a)–(j) and Fig. 10(k)–(t), respectively, where the corals are marked in grey. Comparing the first row of panels against the third row that mark different streamwise locations, but have identical wave phases, it is clear to see the large difference observed locally in panels (a)–(e), where the flow is observed to accelerate substantially as marked by the white-red colours. A similar observation can be made when comparing panels (f)–(j) against panels (p)–(t) in Fig. 10, where the flow accelerates with higher speeds in the vicinity of the corals. Since these panels show the phase-averaged speed, these flow features constitute secondary features emerging as a result of the flow interacting with the coral canopy, which is relatively complex and heterogeneous. While not shown in this discussion explicitly, similar observations were made for the other cases and illustrate the complex secondary flow features that emerge as a consequence of flow and coral canopy interactions. Specifically, despite the modest wave Reynolds number, the heterogeneity within the coral canopy introduces a large heterogeneity in the hydrodynamics within the canopy and is observed to have a substantial impact on the small-scale flow features as discussed in the following section.

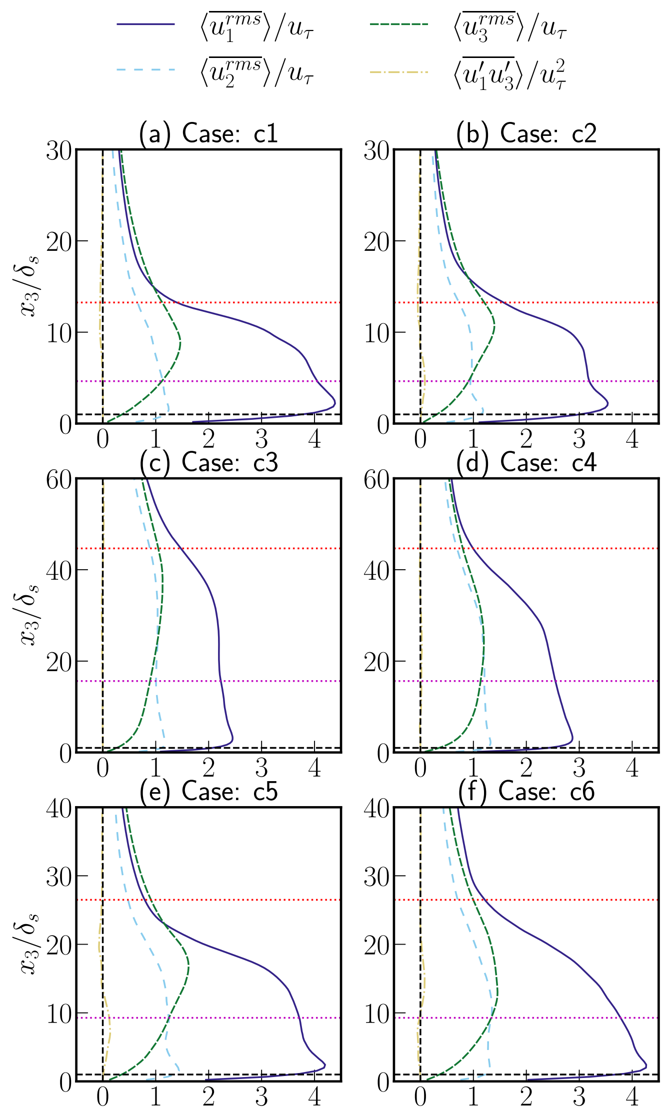


**Fig. 8.** Planform- and time-averaged Reynolds stress and root-mean-squared flow components. The horizontal dashed black line represents the Stokes' boundary layer thickness, while the horizontal dotted magenta line represents $0.35k_s/\delta_s$, and the horizontal dotted red line is $k_s/\delta_s$, i.e., the peak coral height.

### *3.3. Phase averaged turbulence statistics*

As detailed in Appendix A, the TKE dissipation rate ($\langle\epsilon\rangle^*$) is a positive-definite quantity and serves as a sink in the TKE budget, and as seen in Fig. 11, $\langle\epsilon\rangle^*$ scales as expected with $Re_k^b$ and $\Gamma$. In the following sections, TKE dissipation rate refers to the third last term $\left(\frac{\Gamma}{Re_k^b}\langle\widehat{\partial_j u_i' \partial_j u_i'}\rangle\right)$ in Eq. (A.7). Comparing cases c1, c3, c5 against c2, c4, c6 $\langle\epsilon\rangle^*$ is observed to be approximately an order of magnitude different between the two sets of cases. It is important to note that in this representation, $\langle\epsilon\rangle^*$ is scaled using the inertial scaling parameters and not using the inner scaling parameters as would be done conventionally using the kinematic viscosity and the friction velocity for a consistent comparison as detailed in Eq. (A.7). This is also motivated by the fact that it is usually easier to estimate the inertial or outer parameters of the flow as opposed to the inner parameters, thus providing a relatively easier method for a consistent comparison. There is a large peak at the wall, as expected for the oscillatory shear experienced at the bottom wall, and a secondary maximum within the canopy region ($\mathcal{L}_c$), which can be attributed to the coral-induced flow separation. Most of the TKE dissipation is concentrated within the canopy region when the dissipation at the flat wall is ignored for this comparison. This is an important observation as most of the TKE is generated by virtue of the wake production mechanism (Ghodke and Apte, 2018) at a length scale of the coral roughness. Since the representative length scale varies as a function of the coral density, it is expected that most of the TKE dissipation takes place within this canopy region. The magnitude of $\langle\epsilon\rangle^*$ for all cases rapidly falls off to zero above $k_s$. The $\langle\epsilon\rangle^*$ is observed to be relatively symmetric when comparing the periodic forcing where each symmetric phase is observed to demonstrate similar values for $\langle\epsilon\rangle^*$ with only minor differences which can be attributed to the heterogeneity in the forward and backward frontal areas experienced by the flow. In the time-averaged sense, a large amount of TKE dissipation is observed as marked by the thick solid blue line for all the cases, which also explains the large deficit velocities observed in Fig. 5. These results illustrate that even for a synthetically generated coral configuration, most of the energy dissipation occurs within the canopy region, and $\langle\epsilon\rangle^*$ vanishes rapidly above this canopy region unless other generation and/or transport mechanisms are active.

To further show the sensitivity of the coral morphology and the wave period, we consider the time-averaged and vertically integrated TKE dissipation rate over the coral canopy ($\mathcal{L}_c$) as defined in Eq. (14) given by,

$$\langle\overline{\epsilon}\rangle^v = \int_{\mathcal{L}_c} \langle\overline{\epsilon}\rangle dx_3, \tag{15}$$

where the integral is carried out over the canopy height. Since the scaling parameters are known a-priori as detailed in Table 1, the relative strength of $\langle\overline{\epsilon}\rangle_r^v \equiv \langle\overline{\epsilon}\rangle_{cn}^v/\langle\overline{\epsilon}\rangle_{c1}^v$ can be compared against case c1. Here $\langle\overline{\epsilon}\rangle_{cn}^v$ is the time-averaged and vertically integrated TKE dissipation rate for case $cn$, where $n$ corresponds to the case number. Fig. 12 compares the relative magnitude of the TKE dissipation rate ($\langle\overline{\epsilon}\rangle_r^v$) across the six cases considered in this work. For case c1, the relative magnitude is 1 and is shown for illustration purposes. Comparing case c2 against c1, the data suggests that while the scaling should yield identical values of the TKE dissipation rate, there seems to be some dependence on the relative time scales imposed. While the non-dimensional frequencies, as detailed in Table 3, are similar for cases c1 and c2, the TKE dissipation rate is observed to be relatively smaller when compared against case c1 with identical flow parameters ($\Gamma$ and $Re_k^b$). A similar observation can be made when comparing the paired cases with identical flow parameters, such that the cases with a wave period of 5 s are observed to exhibit a relatively higher TKE dissipation rate when compared against the 15 s counterpart with the same flow conditions. An important detail that could help explain these differences is the relatively lower values of $U_b$ and relatively higher values of $k_s$ for the cases that exhibit lower levels of TKE dissipation rate. Overall, the trend for the TKE dissipation rate is in agreement with the scaling using $\Gamma/Re_k^b$ with some deviations on the exact values that can be mainly attributed to the fact that this scaling is agnostic to the frontal and planform areas of the coral canopies used in this context. For example, cases c3 and c4 show a relative increase in the TKE dissipation rate by $\sim \mathcal{O}(10^1)$. Cases c5 and c6 seem to show relatively different behaviour when compared to the expected scaling, and it is unclear from the data as to the cause of this deviation. The expected behaviour for cases c5 and c6 in the TKE dissipation rate is about a fourfold increase when compared to case c1 for the scaling to hold, however, for case c5 the increase in TKE dissipation rate is by a factor of $\sim 2$, while for case c6 there is a drastically attenuated value. Consequently, while the overall trend for relatively larger $Re_k^b$ is consistent, a similar observation cannot be made consistently for smaller values of $Re_k^b$, and further work would be needed to verify this observation.

The TKE as a function of the wave phase is shown in Fig. 13 using the scaling parameter ($U_b^2$). For all the cases discussed in Fig. 13, the magnitude of TKE over the wave phase is observed to be wave-direction agnostic, as demonstrated by comparing the acceleration half-wave

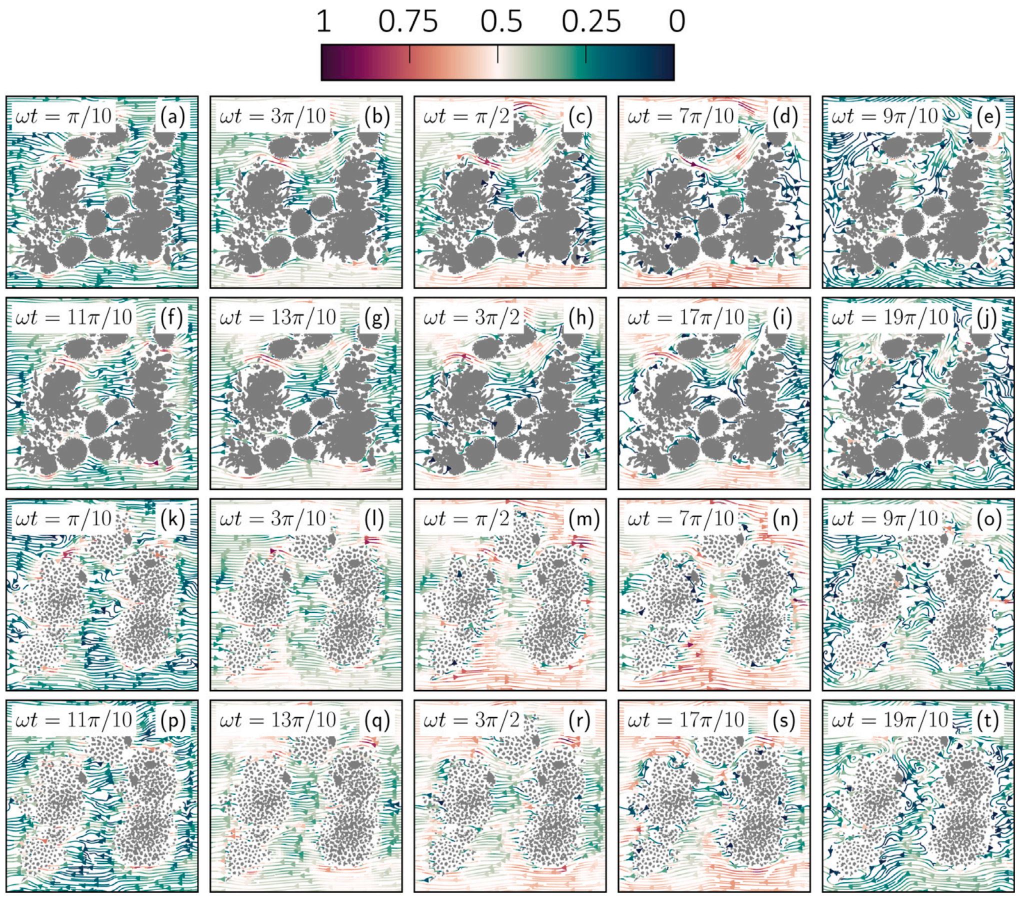


**Fig. 9.** Comparison of the horizontal streamlines comprising the streamwise and the spanwise velocity components at ten waves corresponding to case c5. Panels (a)–(j) show the slice at $x_3/\delta_s = 2.0$ while panels (k)–(t) show the slice at $x_3/\delta_s = 12.0$. The grey colour on all panels marks the coral reef and the colourbar at the top marks the non-dimensional speed $\mathbf{S}/U_b \equiv \left(\sqrt{\widetilde{U}_1^2 + \widetilde{U}_2^2}\right)/U_b$.

cycle against the decelerating part of the half-wave cycle. This is similar to the observations made for the TKE dissipation rate as shown in Figs. 11. Excluding the TKE peak close to the wall, most of the TKE magnitude is concentrated within the canopy region as defined in Eq. (14). Across all the cases discussed in this study, the TKE peak is observed to be located at the mid-way point between the canopy height ($\mathcal{L}_c$), while above the top of the coral canopy, the TKE rapidly decreases to a value that is an order of magnitude smaller when compared to the in-canopy TKE magnitude. These observations suggest that for zero mean sinusoidal flows in shallow environments over dense canopies, most of the TKE and the TKE dissipation rate can is localised to the central portion of the canopy. This can be further illustrated by the variations in the vertical Reynolds stress ($u_1'u_3'$) as detailed in Fig. 14. For all the cases discussed in this study, the peak vertical Reynolds stress is observed to be located within the canopy layer ($\mathcal{L}_c$) as seen by the clustering of the circle markers in Fig. 14. For cases c3, c4, and c5, during some wave phases, the peak vertical Reynolds stress is observed closer to the wall and below the canopy region. As for cases c3 and c4, some of the vertical Reynolds stress peak is sustained slightly above the canopy, which can be understood through the large wave Reynolds number compared to the other cases.

Comparing the peak locations for TKE dissipation rate, TKE, and the vertical Reynolds stress, it is clear that the peaks for all three parameters approximately coincide within the canopy layer. Moreover, the vertical Reynolds stress peaks slightly above the location where the TKE dissipation rate peaks for all the cases, as seen when comparing Figs. 11 and 14. The vertical Reynolds stresses do not exhibit the same wave phase symmetry observed for the TKE dissipation rate and TKE. However, these discrepancies are localised within the vertical direction. For a perfectly symmetric (or sinusoidal) vertical Reynolds stress response, the time-averaged stress integrates to zero for every vertical coordinate. However, as seen in Fig. 14, there is a clear non-zero mean observed for the vertical coordinates until the canopy region. Although locally the vertical Reynolds stress shows a non-zero mean, its vertical integral vanishes, consistent with the lack of a mean flow to balance shear stress over the full canopy-water column. This indicates that the flow has adjusted into a quasi-steady, wave-phase-resolved equilibrium where the spatial variations in Reynolds stress, canopy form drag, and viscous stress collectively balance the time-varying, oscillatory pressure gradient. Above the coral canopy region, all the parameters of interest are an order of magnitude smaller than their in-canopy counterparts, suggesting that the in-canopy aims to set the boundary condition for the flow above it. Close to the flat wall, the vertical Reynolds stress is observed to have the same sign as the streamwise wave orbital velocity ($U_b$), while within the canopy, peaks are observed to have the exact opposite phase dependence. For all the cases, a simultaneous peak was observed close to the wall and within the canopy with opposite magnitudes of the vertical Reynolds stresses. As demonstrated by previous studies (Suzuki et al., 2019; Jacobsen and McFall, 2022; Ascencio et al., 2022; Rooijen et al., 2022), such a dense canopy flow can be modelled effectively using a canopy drag parameterisation where the observations made in this study can provide useful building blocks for tuning the model coefficients. While the drag parameterisation relies on understanding the bulk effect of the canopy

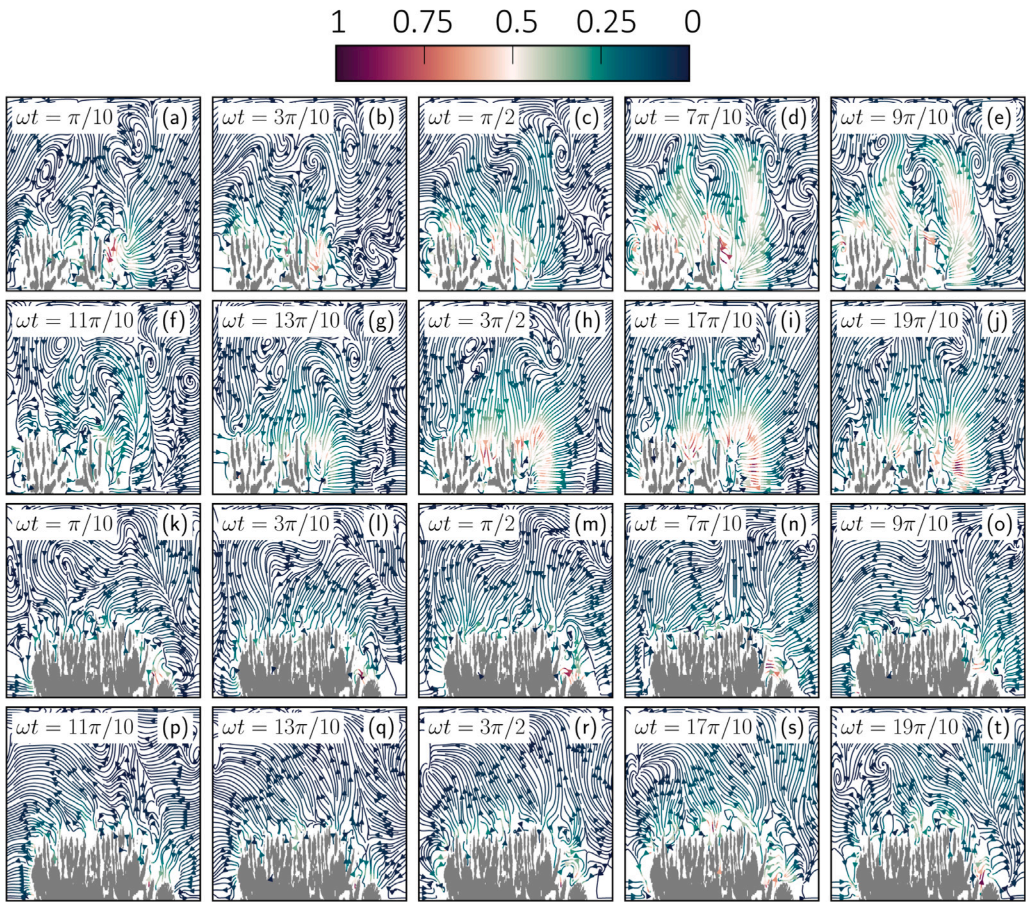


**Fig. 10.** Comparison of the streamlines comprising the spanwise and the vertical velocity components at ten waves corresponding to case c5. Panels (a)–(j) show the slice at $x_1/\delta_s = 24.0$ while panels (k)–(t) show the slice at $x_1/\delta_s = 145.0$. The grey colour on all panels marks the coral reef and the colourbar at the top marks the non-dimensional speed $\mathbf{S}/U_b \equiv \left(\sqrt{\widetilde{U}_2^2 + \widetilde{U}_3^2}\right)/U_b$.

on the flow above it, for unsteady Reynolds Averaged Navier Stokes (URANS) style methods, it can become relevant to model the transport of TKE, where the model coefficients can be tuned based on the specific transport mechanisms. Additionally, as detailed by Conde-Frias et al. (2023), the near-bed TKE and vertical Reynolds stress peaks play a significant role in the transport of momentum, TKE, and sediment. When comparing cases c1 and c2 against c3 and c4, the wave Reynolds number is larger by an order of magnitude for the latter cases. As a result, it is expected that with increasing wave Reynolds number, the region closer to the wall experiences larger vertical Reynolds stresses. This is especially consequential when fine sediment is present at the bottom wall, which can then be entrained during these parts of the wave cycle. The concentration of the TKE and TKE dissipation within the canopy region also suggests that once suspended, there is a larger potential for such sediment to be dispersed within the canopy region. In coastal systems, surface gravity waves can be accompanied by mean currents, which can then transport both TKE and sediment outside the canopy layer. Overall, these findings can provide fruitful insights into the energetics within the canopy region for complex roughness subject to wave motion.

## 4. Conclusions

This study utilised a scalable turbulence-resolving computational framework to model flow around synthetically generated coral reefs over a flat topography. Varied coral canopy parameters were simulated for two wave Reynolds numbers and relative roughness with the aim of better understanding the in-canopy turbulence dynamics. We found that the in-canopy flow is similar for varied coral parameters as long as the free-stream wave orbital velocity is used to normalise the comparison. A weak correlation was observed between the canopy-integrated velocity and the relative roughness; however, given the wide variation in the planform and frontal area for the cases, no discernible conclusions can be made about the overall trend. An important observation in this study suggests that most of the turbulent kinetic energy dissipation occurs within the canopy region, defined as the region between the top of the coral roughness and the location where the spanwise and streamwise root mean squared turbulent velocities are approximately equal to the maximum friction (shear) velocity. Moreover, a similar observation was made for the vertical Reynolds stress, which collectively has broader implications for in-canopy dynamics such as sediment transport, mass transfer rates, and biological activity, to name a few. A weak correlation was also observed between the coral morphology and the turbulent kinetic energy dissipation rate, thus motivating further studies to quantify this connection.

While some interesting observations were made, this study was carried out for a wave Reynolds number that is laminar. Thus, comparisons with in situ conditions cannot be directly made. Additionally, the range of parameters chosen in this work is relatively modest, primarily to limit the introduction of a larger computational cost. Consequently, while these observations provide insights into the small-scale dynamics using a scale-resolving framework, more work is needed to translate

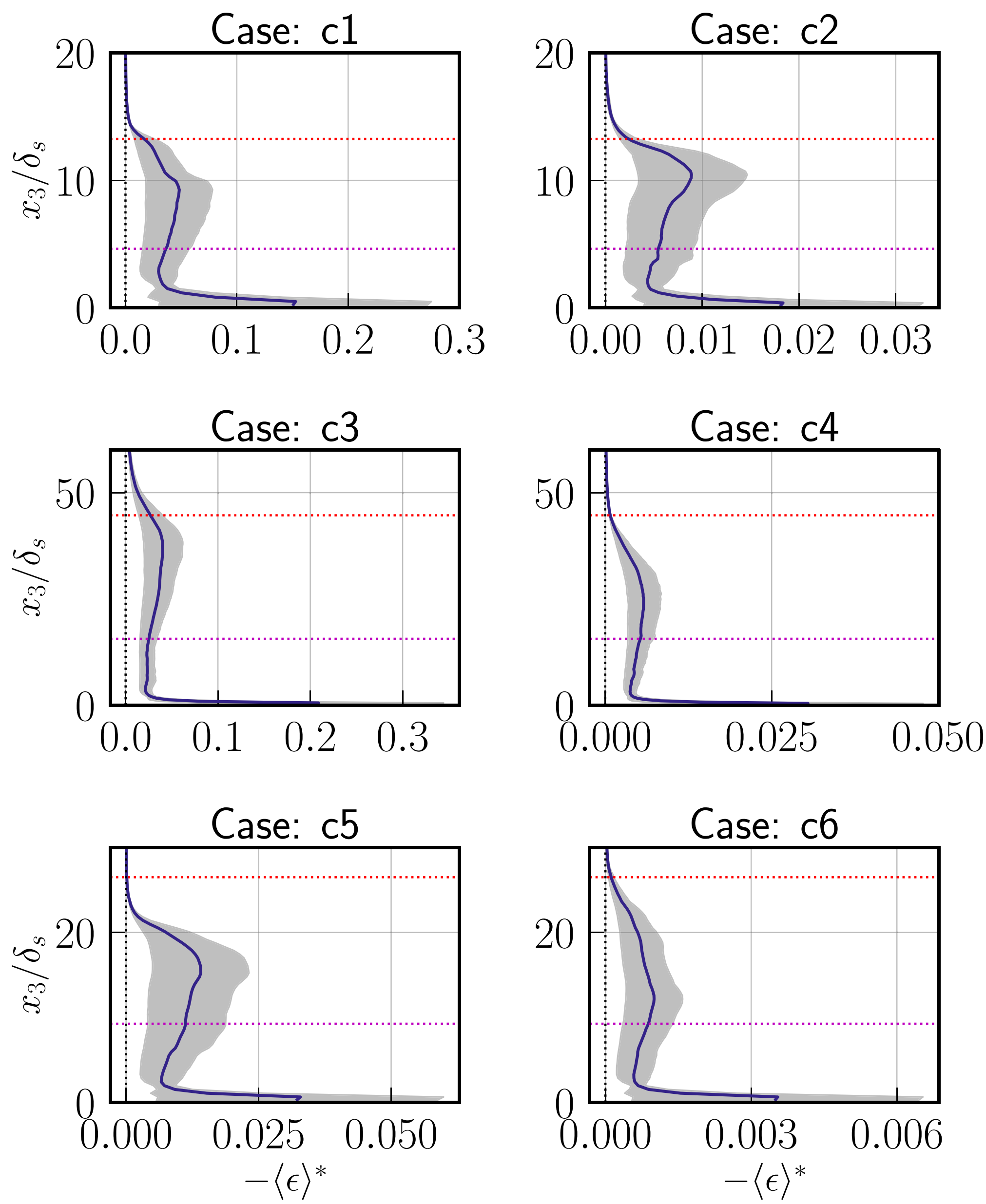


**Fig. 11.** Phase- and planform-averaged TKE dissipation rate where the solid blue line marks the time-averaged value while the grey area marks the variation of TKE dissipation rate over the wave cycle. Here, the non-dimensionalisation is carried out as discussed in Appendix A and denoted by $\langle\epsilon\rangle^*$.

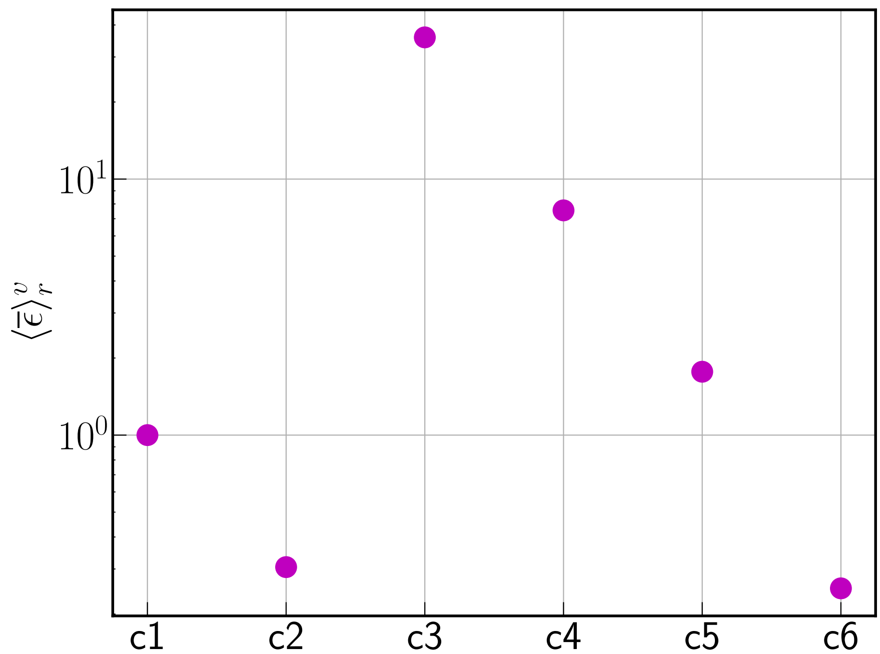


**Fig. 12.** Time-averaged and vertically integrated TKE dissipation rate comparison relative to case c1 for all the cases discussed in this work.

these findings to in situ conditions. In the following future works, a substantial inquiry into first characterising the coral morphology can be envisioned, followed by a detailed numerical inquiry into the connections between the morphology and the hydrodynamics response, which can help bridge the gap in our current understanding of coral reef systems. As a pilot study, this work aimed at adapting the computational framework to study the flow around complex roughness, such as coral reefs, to understand the in-canopy flows. To that end, we find that such a simulation framework can provide further impetus in the development of reduced-order models, leveraging high-fidelity results and providing deeper insights into the flow around complex roughness in coastal oceanic environments.

## Open research section

The stochastic coral bed generator is freely available through the public repository https://github.com/AkshayPatil1994/turbocor.git. The stl2sdf generator can be accessed from the public repository https://github.com/AkshayPatil1994/stl2sdf.git. Some of the generated data can be made available upon a reasonable request submitted to the first author (a total of 5 Tib (Terabytes) of data was generated in this numerical experiment).

## Carbon footprint statement

This work made use of the Snellius supercomputer and had an estimated footprint of 606 kg $CO_2$-equivalent (at least if not higher) using the Green Algorithms (http://calculator.green-algorithms.org/). The input data used to arrive at these estimates was: Runtime - 1472 h, Number of cores - 128, Model AMD EPYC 7h12, and Memory available: 256 GiB, located in the Netherlands. This is equivalent to taking 1.1 flights from New York (U.S.) to San Francisco (U.S.).

## CRediT authorship contribution statement

**Akshay Patil:** Writing – review & editing, Writing – original draft, Visualization, Validation, Software, Methodology, Investigation, Formal analysis, Data curation, Conceptualization. **Clara García-Sánchez:** Writing – review & editing, Resources, Project administration, Methodology, Funding acquisition, Conceptualization.

## Declaration of competing interest

The authors declare that they have no known competing financial interests or personal relationships that could have appeared to influence the work reported in this paper.

## Acknowledgments

This work made use of the Dutch national e-infrastructure with the support of the SURF Cooperative using grant no. EINF-6125, supplemented by the Dutch Research Council (NWO). This publication is part of the project "Unravelling the Turbulence Dynamics: Investigating Wave-Induced Turbulence over Corals" (with project number EINF-6125, which is (partly) financed by the Dutch Research Council (NWO). AP would like to acknowledge the data storage infrastructure provided by the 3D Geoinformation Research Group, Delft University of Technology. AP would like to thank Ivan Pađen for sharing the wrapwrap application and Pedro Costa for their valuable input during the prepartion of this manuscript. While preparing this manuscript, the generative AI tool Grammarly was used to check grammar and sentence structures. After using this tool, the authors reviewed and edited the content as needed and take full responsibility for the content of the publication.

## Appendix A. Derivation of the turbulent kinetic energy budget

Using the velocity decomposition defined in Eq. (9), we can obtain the wave phase- (henceforth, phase-averaged) and planform-averaged momentum equations to derive the phase- and planform-averaged TKE (ppTKE) equation for this flow. Consider the non-dimensional continuity equation with the triple decomposition given by (dropping the functional dependence parentheses and the $*$ notation when compared

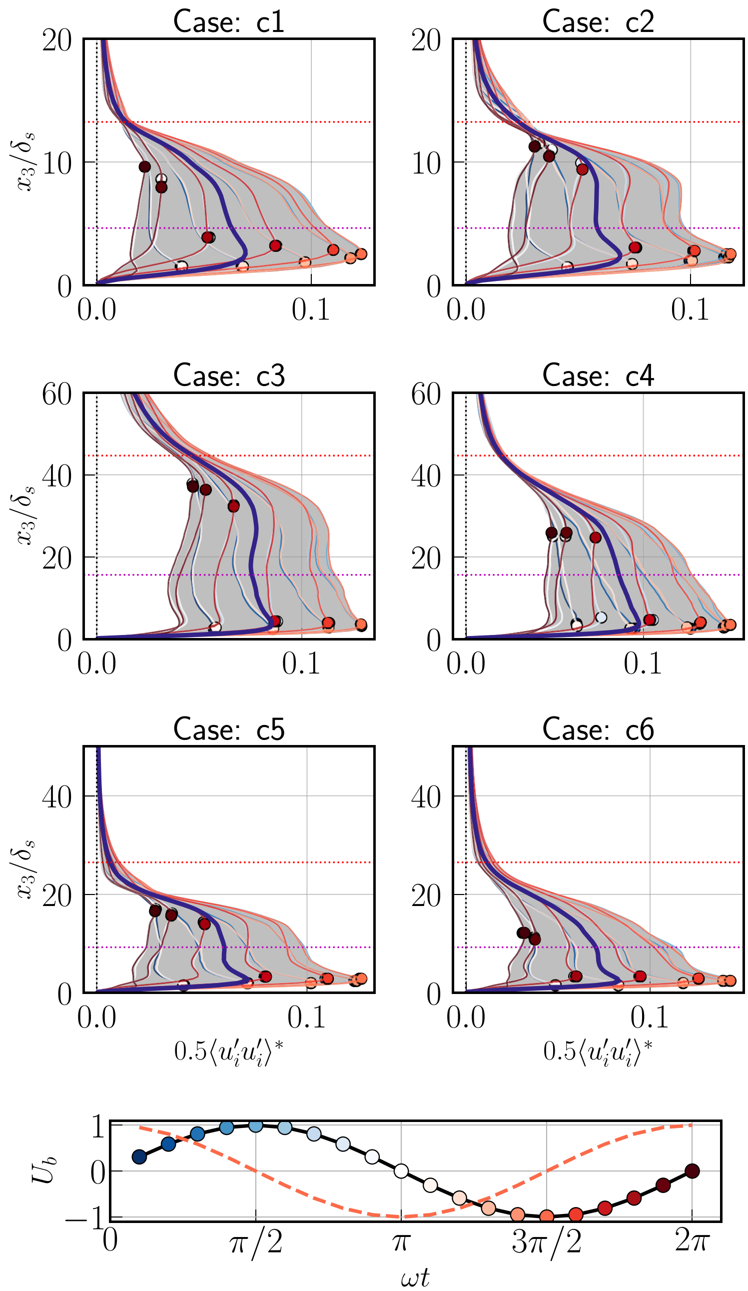


**Fig. 13.** Phase- and planform-averaged TKE as a function of the wave phase marked by the grey shading, while the thick blue line marks the time-averaged vertical profile and the thin coloured lines mark the phase-averaged profiles corresponding to the wave phase marked at the bottom-most panel. Here, the TKE is normalised using the square of the maximum wave orbital velocity ($U_b^2$). The dashed solid line in the bottom most panel corresponds to the driving pressure gradient ($U_b \omega \cos(\omega t)$) while the solid black line corresponds to the wave orbital velocity ($U_b$).

to Eq. (4))

$$\partial_i \langle \widetilde{u}_i \rangle + \partial_i \hat{u}_i + \partial_i u_i' = 0, \tag{A.1}$$

applying the phase- and planform-averaging operators to the equation above results in all the terms vanishing; thus, the continuity equation remains unchanged for this velocity decomposition. It is important to note that the planform-average of the dispersive velocity component is zero by definition (see Eq. (10)) and the periodic boundary conditions in the homogeneous directions suggest that any gradients of flow quantities vanish (i.e., $\partial_1 \langle \cdot \rangle = \partial_2 \langle \cdot \rangle = 0$). This suggests that, independently, the velocity components are divergence-free for incompressible flows.

First, we consider the non-dimensional momentum equations decomposed using the phase-averaged and the turbulent velocity components (i.e., Eq. (7)) given by

$$\partial_t \left(\widetilde{u}_i + u_i'\right) + \Gamma \partial_j \left(\left[\widetilde{u}_j + u_j'\right]\left[\widetilde{u}_i + u_i'\right]\right) = -\Gamma \partial_i \left(\widetilde{p} + p'\right) + \frac{\Gamma}{Re_k^b} \partial_j \partial_j \left(\widetilde{u}_i + u_i'\right) + \cos(t)\delta_{i1}, \tag{A.2}$$

where applying the phase-averaging operator after expanding the quadratic non-linear term gives

$$\partial_t \widetilde{u}_i + \Gamma \partial_j \widetilde{\widetilde{u}_j \widetilde{u}_i} = -\Gamma \partial_i \widetilde{p} + \frac{\Gamma}{Re_k^b} \partial_j \partial_j \widetilde{u}_i - \Gamma \partial_j \widetilde{u_j' u_i'} + \cos(t)\delta_{i1}, \tag{A.3}$$

the equation above is the phase-averaged momentum equation where the energy at the inertial scale is injected by the cosine forcing (i.e., last term on the right-hand side). The turbulent kinetic energy equation can

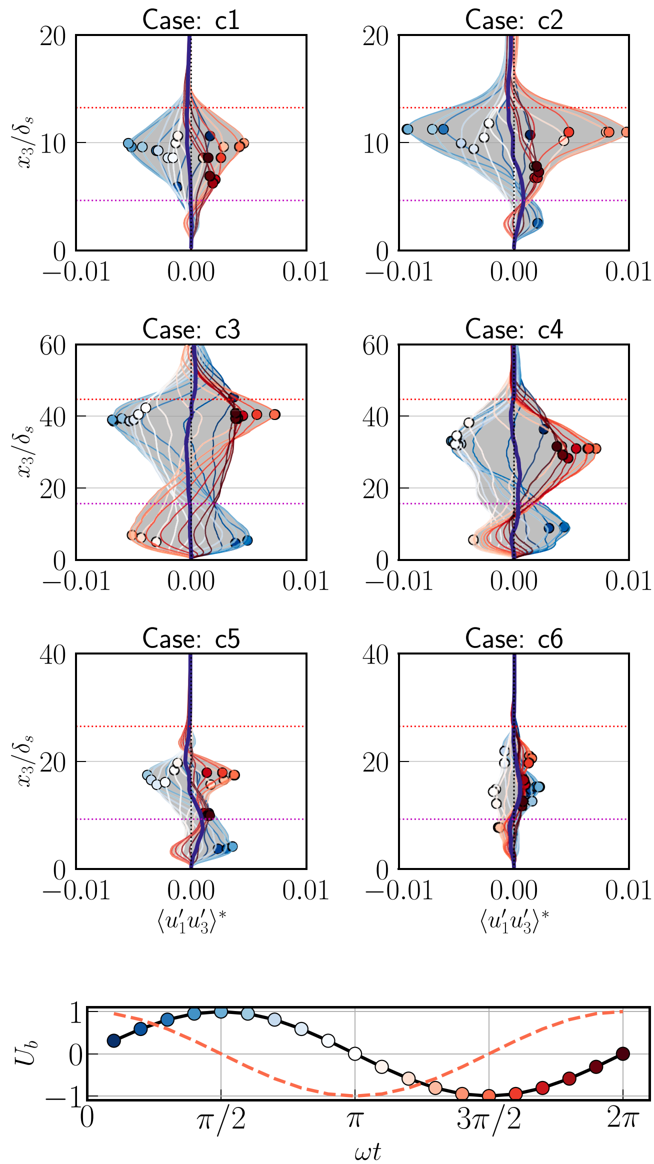


**Fig. 14.** Phase- and planform-averaged vertical Reynolds stress $\langle u_1' u_3' \rangle$ as a function of the wave phase marked by the grey shading, while the thick blue line marks the time-averaged vertical profile and the thin coloured lines mark the phase averaged profiles corresponding to the wave phase marked at the bottom-most panel. Filled circles mark the maximum value of $\langle u_1' u_3' \rangle$ for the corresponding wave phase marked in the bottom-most panel with identical colour coding. Here, the stress terms are normalised using the square of the maximum wave orbital velocity ($U_b^2$). The dashed solid line in the bottom most panel corresponds to the driving pressure gradient ($U_b \omega \cos(\omega t)$) while the solid black line corresponds to the wave orbital velocity ($U_b$).

be derived by subtracting Eq. (A.3) from the momentum equation in its decomposed form and multiplying the residual equation by $u_i'$ to give

$$
\begin{aligned}
&\partial_t u_i' u_i' + \Gamma \partial_j \tilde{u}_j u_i' u_i' + \Gamma u_i' \partial_j \tilde{u}_j \tilde{u}_i \\
&+ \Gamma u_i' u_j' \partial_j \tilde{u}_j + \frac{\Gamma}{2} \partial_j u_j' u_i' u_i' + \Gamma u_j' \partial_j \widetilde{\tilde{u}_j \tilde{u}_i} \\
&= -\Gamma \partial_i p' u_i' - \Gamma u_i' \partial_j \widetilde{u_j' u_i'} \\
&+ \frac{\Gamma}{2 Re_k^b} \partial_j \partial_j u_i' u_i' - \frac{\Gamma}{Re_k^b} \partial_j u_i' \partial_j u_i',
\end{aligned} \tag{A.4}
$$

applying the phase-averaging operator to the equation above yields the TKE equation given by

$$
\begin{aligned}
D_t \tilde{k} = &-\Gamma \widetilde{u_i' u_j'} \partial_j \tilde{u}_i - \frac{\Gamma}{Re_k^b} \partial_j \widetilde{u_i' \partial_j u_i'} + \frac{\Gamma}{Re_k^b} \partial_j \partial_j \tilde{k} \\
&- \Gamma \partial_j \widetilde{u_j' k} - \Gamma \partial_i \widetilde{p' u_i'}
\end{aligned} \tag{A.5}
$$

where the terms in order are the total rate of change of TKE (i.e., operator defined as $D_t \equiv \partial_t + \Gamma \partial_j \tilde{u}_j$), production of TKE by phase-averaged wave shear, TKE dissipation rate, TKE diffusion by viscosity, turbulent transport of TKE, and pressure-velocity correlations, respectively. It is important to note that, as the terms are phase-averaged, they represent the instantaneous TKE balance at a given wave phase. The above derivation uses the identity.

$$
\widetilde{\tilde{f} \tilde{g}} = \tilde{f} \tilde{g} - \overline{\tilde{f} \tilde{g}}, \tag{A.6}
$$

where $f$ and $g$ are two flow quantities. The ppTKE equation can now be derived by substituting the velocity decomposition for the phase-averaged component defined in Eq. (10) to give

$$
\begin{aligned}
D_t \langle \tilde{k} \rangle = &- \Gamma \langle \widetilde{u_i' u_j'} \rangle \partial_j \langle \tilde{u}_i \rangle - \frac{\Gamma}{Re_k^b} \langle \widetilde{\partial_j u_i' \partial_j u_i'} \rangle \\
&+ \frac{\Gamma}{Re_k^b} \partial_j \partial_j \langle \tilde{k} \rangle - \Gamma \partial_j \langle \widetilde{u_j' k} \rangle - \Gamma \partial_i \langle \widetilde{p' u_i'} \rangle \\
&- \Gamma \langle \widehat{u_i' u_j'} \rangle \partial_j \langle \tilde{u}_i \rangle - \frac{\Gamma}{Re_k^b} \langle \widehat{\partial_j u_i' \partial_j u_i'} \rangle \\
&- 2\Gamma \partial_j \langle \widehat{u_j' k} \rangle - \Gamma \partial_i \langle \widehat{p' u_i'} \rangle
\end{aligned} \tag{A.7}
$$

where the terms in order are the total rate of change of ppTKE, ppTKE production by Reynolds-stress and wave shear, ppTKE rate of dissipation, diffusion of ppTKE by viscosity, turbulent transport of ppTKE, pressure-velocity correlations, production of ppTKE by dispersive stresses and wave shear, ppTKE rate of dissipation through dispersive stresses, dispersive component of the turbulent transport of ppTKE, and the dispersive component of the pressure-velocity correlations, respectively.

## Appendix B. Scaling test for the signed-distance-field generator

The signed-distance-field (SDF) generator named stl2sdf was implemented in pure Python and scales up to 2 billion grid cells over 32 CPUs with a peak memory requirement of approximately 50 Gib for a geometry file of size 57 MiB in total. Table B.4 presents the scaling results for a coral bed where the analysis time represents the time spent on the parallel portion of the code to compute the SDF, and the total time spent represents the total time spent by the code, including the MPI initialisation and file I/O. Fig. B.15 shows the linear scaling as expected for an SDF algorithm that is easily parallelised, as there is no communication between the various domains. The parallelisation uses a simple slab-type decomposition along the $x_1$ flow direction, as this is usually the longest dimension in a channel-type flow simulation, where stl2sdf is mostly used. The peak memory usage on the right panel indicates sufficiently low memory requirements for a parallel workflow for a limited size of the geometry input. It is important to note that using more cores in stl2sdf can increase the memory requirement non-trivially, as the trimesh library (Dawson-Haggerty et al., 2019) used to handle the geometry creates $N$-copies of the geometry when using $N$-processors during the Message-Passing-Interface (MPI) broadcast directive. Despite these minor limitations, the code scales excellently and has been tested for 2 billion grid points in the computational domain with similar performance and memory requirements for linearly scaled geometry and nsamples.

## Data availability

Data will be made available on request.

**Table B.4**
Scaling results for generating the SDF for a coral bed with 536.8 million grid cells with 5 million sampling points around the geometry.

| Number of processors | Analysis time [s] | Total time [s] | Peak memory usage [GiB] |
|---|---|---|---|
| 1 | 22 584.0 | 22 611.8 | 20 |
| 2 | 11 244.5 | 1138.2 | 22 |
| 4 | 5476.5 | 5811.7 | 26 |
| 8 | 2723.0 | 3014.5 | 32 |
| 16 | 1243.8 | 1552.9 | 43 |
| 32 | 627.7 | 846.9 | 52 |

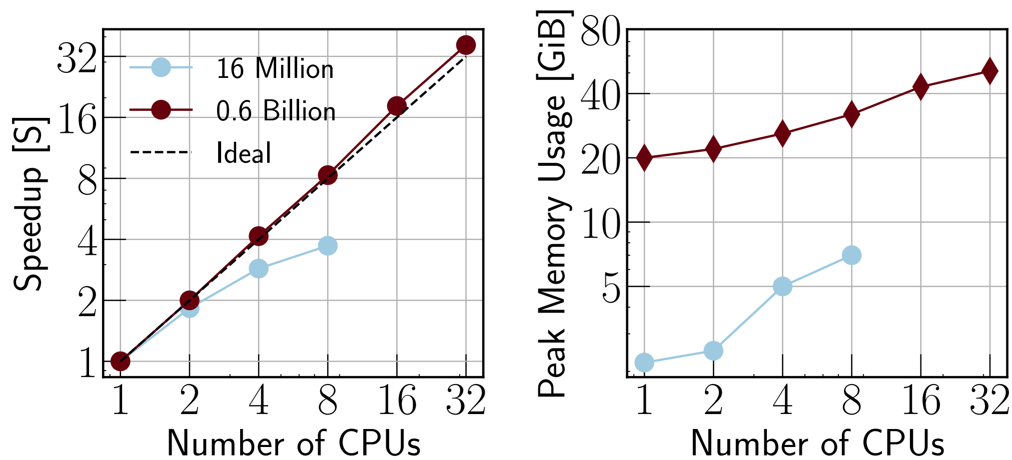


**Fig. B.15.** Strong scaling for stl2sdf along with the peak memory usage as detailed in Table B.4, along with a smaller scale for comparison. The numbers in the legend correspond to the total number of grid cells for the case.

## References


Alliez, P., Cohen-Steiner, D., Hemmer, M., Portaneri, C., Rouxel-Labbé, M., 2023. 3D alpha wrapping. In: CGAL User and Reference Manual. 5.6 Ed. CGAL Editorial Board, p. p. 1.

Ascencio, J.A., Jacobsen, N.G., McFall, B.C., Groeneweg, J., Vuik, V., Reniers, A.J., 2022. Evaluation of implicit and explicit wave dissipation models for submerged and emergent aquatic vegetation. J. Coast. Res. 38, 807–815.

Caldeira, K., Wickett, M.E., 2003. Anthropogenic carbon and ocean ph. Nature 425, 365–365.

Conde-Frias, M., Ghisalberti, M., Lowe, R.J., Abdolahpour, M., Etminan, V., 2023. The near-bed flow structure and bed shear stresses within emergent vegetation. Water Resour. Res. 59, e2022WR032499.

Dawson-Haggerty, et al., 2019. Trimesh. https://trimesh.org/.

Dunbar, D., van der, .D.A., Scandura, P., O'Donoghue, T., 2023. An experimental and numerical study of turbulent oscillatory flow over an irregular rough wall. J. Fluid Mech. 955 (A33), http://dx.doi.org/10.1017/jfm.2022.1090.

Falter, J.L., Atkinson, M.J., Coimbra, C.F.M., 2005. Effects of surface roughness and oscillatory flow on the dissolution of plaster forms: Evidence for nutrient mass transfer to coral reef communities. Limnol. Oceanogr. 50, 246–254.

Ghisalberti, M., Nepf, H.M., 2002. Mixing layers and coherent structures in vegetated aquatic flows. J. Geophys. Res. 107 (C2), http://dx.doi.org/10.1029/2001JC000871.

Ghodke, C.D., Apte, S.V., 2016. DNS study of particle-bed–turbulence interactions in an oscillatory wall-bounded flow. J. Fluid Mech. 792, 232–251.

Ghodke, C.D., Apte, S.V., 2018. Roughness effects on the second-order turbulence statistics in oscillatory flows. Comput. & Fluids 162, 160–170.

Hearn, C., Atkinson, M., Falter, J., 2001. A physical derivation of nutrient-uptake rates in coral reefs: Effects of roughness and waves. Coral Reefs 20, 347–356.

Jacobsen, N.G., McFall, B.C., 2022. Wave-averaged properties for non-breaking waves in a canopy: Viscous boundary layer and vertical shear stress distribution. Coast. Eng. 174, 104117.

Jelly, T.O., Chin, R.C., Illingworth, S.J., Monty, J.P., Marusic, I., Ooi, A., 2020. A direct comparison of pulsatile and non-pulsatile rough-wall turbulent pipe flow. J. Fluid Mech. 895 (3).

Jiménez, J., 2004. Turbulent flows over rough walls. Annu. Rev. Fluid Mech. 36, 173–196.

Jones, N.L., Lowe, R.J., Pawlak, G., Fong, D.A., Monismith, S.G., 2008. Plume dispersion on a fringing coral reef system. Limnol. Oceanogr. 53, 2273–2286.

Lacy, J.R., MacVean, L.J., 2016. Wave attenuation in the shallows of San Francisco Bay. Coast. Eng. 114, 159–168.

Lowe, R.J., Falter, J.L., 2015. Oceanic forcing of coral reefs. Annu. Rev. Mar. Sci. 7, 43–66.

McKenney, A., Greengard, L., Mayo, A., 1995. A fast Poisson solver for complex geometries. J. Comput. Phys. 118, 348–355. http://dx.doi.org/10.1006/jcph.1995.1104.

Moin, P., Verzicco, R., 2016. On the suitability of second-order accurate discretizations for turbulent flow simulations. Eur. J. Mech. B Fluids 55, 242–245.

Monismith, S.G., 2007. Hydrodynamics of coral reefs. Annu. Rev. Fluid Mech. 39, 37–55.

Monti, A., Omidyeganeh, M., Eckhardt, B., Pinelli, A., 2020. On the genesis of different regimes in canopy flows: a numerical investigation. J. Fluid Mech. 891 (A9).

Munk, W.H., Sargent, M.C., 1948. Adjustment of bikini atoll to ocean waves. Trans. Am. Geophys. Union 29 (855).

Nepf, H.M., 2011. Flow and transport in regions with aquatic vegetation. Annu. Rev. Fluid Mech. 44, 123–142.

Nepf, H.M., Vivoni, E.R., 2000. Flow structure in depth-limited, vegetated flow. Journal Geophysical Research 105, 547–575.

Nielsen, P., 1992. Coastal bottom boundary layers and sediment transport., vol. 4, World scientific.

Nunes, V., Pawlak, G., 2008. Observations of bed roughness of a coral reef. J. Coast. Res. 2, 39–50.

Orlandi, P., 2000. Fluid Flow Phenomena. In: Fluid Mechanics and Its Applications, Vol. 55, Springer Netherlands, Dordrecht.

Ozdemir, C.E., Hsu, T.J., Balachandar, S., 2014. Direct numerical simulations of transition and turbulence in smooth-walled stokes boundary layer. Phys. Fluids 26.

Perlin, K., 1985. An image synthesizer. ACM Siggraph Comput. Graph. 19, 287–296.

Pomeroy, A.W., Ghisalberti, M., Peterson, M., Farooji, V.E., 2023. A framework to quantify flow through coral reefs of varying coral cover and morphology. PLoS ONE 18, 00.

Pope, S.B., 2000. Turbulent Flows. Cambridge University Press.

Pujol, D., Casamitjana, X., Serra, T., Colomer, J., 2013. Canopy-scale turbulence under oscillatory flow. Cont. Shelf Res. 66, 9–18.

Reidenbach, M.A., 2004. Boundary Layer Dynamics in Coral Reef Systems (Ph.D. thesis). Stanford University, Copyright - Database copyright ProQuest LLC; ProQuest does not claim copyright in the individual underlying works; Last updated - 2023-03-02.

Reidenbach, M.A., Monismith, S.G., Koseff, J.R., Yahel, G., Genin, A., 2006. Boundary layer turbulence and flow structure over a fringing coral reef. Limnol. Oceanogr. 51, 1956–1968.

Ribes, M., Atkinson, M.J., 2007. Effects of water velocity on picoplankton uptake by coral reef communities. Coral Reefs 26, 413–421.

Rooijen, A.van, Lowe, R., Ghisalberti, M., McCall, R., Hansen, J., 2022. Modelling wave attenuation through submerged vegetation canopies using a subgrid canopy flow model. Coast. Eng. 176, 104153.

Scotti, A., 2006. Direct numerical simulation of turbulent channel flows with boundary roughened with virtual sandpaper. Phys. Fluids 18, 031701.
Selmoni, O., Cleves, P.A., Exposito-Alonso, M., 2024. Global coral genomic vulnerability explains recent reef losses. bioRxiv.
Stokes, G., 1851. On the effect of the internal friction of fluids on the motion of pendulums. Trans. Camb. Phil. Soc 9 (8).
Suzuki, T., Hu, Z., Kumada, K., Phan, L.K., Zijlema, M., 2019. Non-hydrostatic modeling of drag, inertia and porous effects in wave propagation over dense vegetation fields. Coast. Eng. 149, 49–64.
Taylor, G.I., 1938. The spectrum of turbulence. Proc. R. Soc. Lond. Ser. A- Math. Phys. Sci. 164, 476–490.
Yuan, J., Piomelli, U., 2015. Numerical simulation of a spatially developing accelerating boundary layer over roughness. J. Fluid Mech. 780, 192–214.